Revision 1

Mineralogy of the 1.45 Ga Wafangzi manganese deposit in North China: Implications for pulsed Mesoproterozoic oxygenation events

Hao Yan [1], Lingang Xu [2*], Jingwen Mao [2], Dongjie Tang [1], Xiuqing Yang [3], Yinzeng Bai [4], Chao Li [4], Kurt O. Konhauser [5], Leslie J. Robbins [6]

[1] Institute of Earth Sciences, China University of Geosciences, Beijing, China

[2] School of Earth Sciences and Resources, China University of Geosciences, Beijing, China

[3] MOE Key Laboratory of Western China's Mineral Resources and Geological Engineering, School of Earth Science and Recourses, Chang'an University, Xi'an, China

[4] Liaoning Province Nonferrous Geology 109 Team Co. Ltd, Liaoning, China

[5] Department of Earth & Atmospheric Sciences, University of Alberta, Edmonton, AB, Canada

[6] Department of Geology, University of Regina, Regina, SK, Canada

Corresponding author: xulingang@cugb.edu.cn

Abstract

Ancient manganese (Mn) deposits are primarily characterized by the presence of Mn(II) carbonates that likely formed by the diagenetic reduction of precursor Mn(IV) oxides. As such, Precambrian sedimentary Mn deposits have been used as a line of evidence for the evolution of oxygen in Earth's surface environments. However, recent studies have shown that these Mn(II)-carbonates have the ability to directly accumulate within anoxic water columns, where free oxygen does not play a role in their formation. This alternative pathway casts uncertainty on the robustness of using ancient Mn deposits to constrain the redox fabric of the past marine water columns. Here, we investigate the Wafangzi Mn and Fe ore deposit from the 1.45 billion-year-old Tieling Formation, North China. The deposit contains Mn(II,III) mineral phases (hausmannite, braunite) as inclusions, or unreacted residues, trapped within Mn(II) carbonate (Ca-rhodochrosite). Some nodules and oolites of Mn(II) and Fe(II)-carbonate phases are also present and display a banded structure with concentric rings. Mn(III) oxide (manganite) is present in a paragenetic assemblage along with hematite and replacement textures with braunite. The negative carbon isotope composition (δ^{13}C, -7‰ to -4‰) from Mn(II) carbonate samples in the Wafangzi Mn deposit which are distinct from that of contemporaneous seawater (~0‰), along with petrographic and speciation analyses, collectively suggest that the Mn(II,III)- and Fe(II)-bearing mineral phases formed through the diagenetic reduction of primary Mn(IV)/Fe(III) minerals coupled to the oxidation of organic matter. Therefore, the Wafangzi Mn deposit suggests the presence of sufficiently oxygenated marine waters, overlying anoxic ferruginous deeper waters with a transitional manganous water layer that could have driven the redox cycling of Mn, Fe, and C. Given the contemporaneous economic Mn deposits in the 1.45 Ga Ullawarra Formation in Western Australia, our findings imply the existence of a transient, and perhaps widespread, pulsed oxygenation event in the mid-Proterozoic oceans.

Keywords: Mesoproterozoic, Manganese deposit, Manganese and Iron cycle, Redox, Oxygenation

Introduction

Manganese (Mn) is a strongly redox-dependent element, with a high redox potential that requires the presence of dissolved O_2 for the effective oxidation of Mn(II) to form Mn(III,IV) oxides (Tebo et al. 2004; Morgan 2005; Dick et al. 2009; Maynard 2010; Hansel et al. 2012; Planavsky et al. 2014a; Johnson et al. 2016a; Lingappaa et al. 2019; Robbins et al. 2023). The traditional metallogenic model for large, economic stratiform Mn deposits assumes that the Mn(II) minerals (either carbonates or silicates) now present are the diagenetic products of primary Mn(IV) oxide reduction (Calvert and Pedersen 1996; Van Cappellen and Wang 1996; Maynard 2010; Johnson et al. 2016a; Yan et al. 2022). Therefore, Mn deposition within ancient sediments is generally regarded as a strong indicator for the presence of highly oxidized environments (i.e., the presence of free O_2) in Earth's early surface environments, namely the atmosphere and oceans (Roy 2006; Maynard 2010; Planavsky et al. 2014a; Johnson et al. 2016a;

Johnson 2019; Ostrander et al. 2019; Yan et al. 2022).

In general, the distribution of Precambrian economic Mn deposits is temporally related to the Great Oxidation Event (GOE) and Neoproterozoic Oxidation Event (NOE), times when Earth's atmosphere became progressively more oxygenated (Fig. 1; Roy 2006; Bekker et al. 2014; Maynard 2010). By contrast, a pronounced hiatus in Mn deposition on a global scale appears coincident with the mid-Proterozoic (1.8 to 0.8 Ga), the intervening period between the GOE and NOE, which has been historically defined as time of limited oxygenation (Fig. 1; e.g., Canfield 1998; Holland 2006; Planavsky et al. 2011, 2014b, 2018; Reinhard et al. 2013; Partin et al. 2013; Lyons et al. 2014; Cole et al. 2016; Tang et al. 2016; Bellefroid et al. 2018; Diamond et al. 2018).

Recent geochemical studies, however, suggest that the mid-Proterozoic may have been more dynamic than previously recognized, with the existence of at least transient oxygenated marine environments (e.g., Gilleaudeau et al. 2016; Zhang et al. 2016, 2017, 2019, 2022; Canfield et al. 2018, 2021; Diamond and Lyons 2018; Tang et al. 2018, 2020; Zhang et al. 2018; Large et al. 2019; Shang et al. 2019; Liu et al. 2020a; Wang et al. 2020; Yu et al. 2022). Especially noteworthy is the recent identification of economic Mn deposits in the 1.58 Ga Gaoyuzhuang Formation in North China, and 1.45 Ga Ullawarra and 1.11 Ga Ilgarari formations in Western Australia. These deposits cast doubt on a Mn hiatus throughout the entire mid-Proterozoic, and provide evidence for at least transient marine oxygenation events (Fig. 1; Fan et al. 1992, 1999; Fang et al. 2020; Spinks et al. 2023). Yet, directly linking deposition of these Mn deposits to environmental oxygenation is complicated by a recently identified alternative depositional pathway where Mn(II) carbonates precipitated within an anoxic water column (Manceau and Gallup 2005; Brusnitsyn et al. 2017; Herndon et al. 2018; Siahi et al. 2020; Wittkop et al. 2020; Gao et al. 2021; Chen et al. 2022). In sum, the fidelity of ancient Mn deposits as reliable proxies for examining the oxidized paleoenvironmental conditions depends on a better understanding of the paragenesis of Mn-bearing minerals.

To verify the robustness of mid-Proterozoic Mn deposits as proxies for oxygenated conditions, this study systematically investigated the Wafangzi Mn deposit hosted in the ~1.45 Ga Tieling Formation in the Yanliao Basin, North China. This deposit is of significant interest as it not only comprises two dispersed Mn ore belts with a variety of Mn-bearing minerals, including oxides, carbonates, and silicates (Fan et al. 1992, 1999), but it is also contemporaneous with the 1.45 Ga Ullawarra Mn belt in Western Australia (Spinks et al. 2023).

Previous studies on Mn deposits have generally relied upon whole rock geochemistry to constrain the formation process for Mn(II) minerals (e.g., Maynard 2010; Zhang et al. 2020; Dong et al. 2023). However, due to the diversity of minerals in Mn ores, many of which have terrigenous clastic components, geochemical analyses alone may lead to several plausible explanations. In this regard, petrographic observations provide the paragenetic context required to elucidate the most parsimonious depositional model that fits bulk geochemical data (e.g., Johnson et al. 2016a; Yan et al. 2022). This study evaluates the paragenesis of various minerals using a combination of petrographic observations and scanning electron microscopy (SEM) over a range of scales. Energy dispersive spectrum (EDS) mapping and Laser Raman spectroscopy (LRS) are further used to evaluate the chemical composition of these minerals. These petrographic and mineralogical observations are then coupled with X-ray photoelectron spectroscopy (XPS) analyses to characterize the redox speciation of Mn mineral phases. When combined with the C isotope composition ($\delta^{13}C_{carb}$), major element and total organic carbon (TOC) contents of ore samples, our results provide the means to interpret the processes underpinning the formation of the Wafangzi Mn deposit. Importantly, our results presented here not only provide new insights into the formation of the Wafangzi Mn deposit, but potentially widespread mid-Proterozoic redox conditions.

2. Geological setting

2.1 Regional geology and geochronology

The North China Craton was established at the end of the Archean, before experiencing rifting, subduction, and accretion during the Paleoproterozoic and Mesoproterozoic (Zhao and Zhai 2013; Zhai et al. 2020). Orogenesis along the margin of the North China Craton is believed to have been the result of the break-up of the supercontinent Columbia (Nuna) and the subsequent formation of Rodinia (Zuo et al. 2019; Zhai et al. 2020). The Yanliao Basin is located at the northern margin of the North China Craton (Fig. 2b), and features some of the most complete, and best-preserved, mid-Proterozoic stratigraphic successions globally, with a maximum thickness of ~9000 m (Fig. 2c; Lu et al. 2002; Meng at al. 2011). This sedimentary succession comprises the

Paleoproterozoic Changcheng Group (~1.66–1.60 Ga), Mesoproterozoic Jixian Group (~1.60–1.40 Ga), and the unconformably overlying Neoproterozoic Qingbaikou Group (~1.00–0.78 Ga).

The Changcheng Group records a series of shallow marine clastic and carbonate assemblages and encompasses, in ascending order, the Changzhougou, Chuanlinggou, Tuanshanzi, and Dahongyu formations. This group is widely distributed and attains a thickness of more than 2600 m (e.g., Lin et al. 2019). The Jixian Group, with a thickness of about 6000 m, consists in ascending order of the Gaoyuzhuang, Yangzhuang, Wumishan, Hongshuizhuang, and Tieling formations. The Jixian Group is dominated by carbonates in the lower section and an assemblage of shale, argillaceous dolomite, and sandstone up section (e.g., Qu et al. 2014). The Qingbaikou Group is less than 400 m thick and consists of the Longshan Formation and overlying Jingeryu Formation, which are mainly composed of sandstone, shale, and minor carbonate (e.g., Tang et al. 2016). It is noteworthy that the Xiamaling Formation lies disconformably between the underlying Tieling Formation and overlying Longshan Formation. This unit consists mainly of dark siltstone, black shales, and iron formation (e.g., Zhang et al. 2016). The whole succession, exposed in the Yanliao Basin, has suffered minimal alternation by hydrothermal fluids and only low-grade metamorphism, generally below prehnite – pumpellyite facies (Li et al. 2003; Chu et al. 2007).

In the last decade, high-precision zircon U-Pb ages have been obtained from the Proterozoic succession of the North China platform, providing a geochronologic framework. Notably, the middle part of the Tieling Formation has been dated at 1437 ±

21 Ma (Su et al. 2010), while the lower part of the Xiamaling Formation has been dated to 1392 ± 1 Ma, by SHRIMP and TIMS Zircon U-Pb ages, respectively (Zhang et al. 2015). Based on these radiometric ages and the stratigraphic relationships between these units, the top of the Tieling Formation can be assigned an age of circa 1400 Ma and the base of this unit should be no older than 1450 Ma (Fig. 2c).

Paleogeographic reconstructions suggest that the Yanliao Basin captures the transition from deep to shallow water conditions (Fig. 2d; Lyu et al. 2021). The Tieling Formation, in the representative sections, including the Xiahuayuan, Jixian, Beizhangzi and Liujiagou sections can be divided into two members, the lower Daizhuangzi (DZZ) and upper Laohuding (LHD) members (Fig. 2e). The DZZ Member (~153 m) is a set of manganiferous dolomites with thin-beds of intercalated manganiferous and potassium-rich shales. The overlying LHD Member (~181 m) is comprised of stromatolitic limestones with dolomitic limestones or dolomites developed in the lower and upper sections. The DZZ Member is interpreted to have been deposited in a deep subtidal to intertidal environment, while the LHD Member was deposited in a shallow subtidal to intertidal setting (Mei et al. 2008; Hardisty et al. 2017; Tang et al. 2017; Wei et al. 2021; Yu et al. 2022).

2.2 The Wafangzi Deposit

Although Mn-rich strata are generally developed in the lower member of the Tieling Formation, they trend to thicken in shallow water conditions, and mineralization is only locally developed along the northeastern margin of the Yanliao Basin in a near-shore depositional environment (Fig. 2e). The Tieling Mn deposits comprise a group of ore bodies that form a belt and include the Wafangzi deposit in the east, the central Taipinggou deposit, and the Zhongxincun deposit in the west (Fig. 3a; Fan et al. 1992, 1999). Among them, the Wafangzi Mn deposit, located in Chaoyang County, is the largest and covers a region of 80 km^2. The Wafangzi Mn ores have a mean concentration of 27.8 wt% MnO and 16.7 wt% FeO. Ore reserves are estimated to be on the order of 37.66 million metric tons (Fan et al. 1992, 1999). The sedimentary sequence exposed in the Wafangzi Mn deposit consists of the mid-Proterozoic Wumishan, Hongshuizhuang, and Tieling formations, and overlying Cambrian sedimentary and Jurassic-Cretaceous volcanic-sedimentary units. The Tieling Formation in the Wafangzi mine area is divided into three parts. The lower part (~35 m) consists of laminated dolostone overlain by three thin layers or lenses of quartzite that display cross bedding. The middle section (~22 m) is the Mn-bearing sequence and is overlain by the upper section, which consists of thick beds of siliceous limestone. The ore-bearing sequence is composed of three Mn ore beds. The thickness of the first and second ore beds (from the bottom up) varies between 0.5-1 m and ~2 m, respectively. The topmost ore bed is thinner and more variable in thickness, averaging ~1 m (Fig. 4).

Notably, different from the Taipinggou and Zhongxincun deposits - which are dominated by Mn-carbonate minerals - the Wafangzi Mn deposit has been divided into southeastern (SE) and northwestern (NW) regional belts by the Niufendongzi fault (Fig. 3b; Fan et al. 1999). The ore-bearing sequence displays both lithological and mineralogical differences between the southeast and northwest belts. The southeast ore belt is composed of red and dark-brown mudstone, interbedded with the ores, and characterized by a mineral assemblage dominated by Mn(III)-oxide and Mn(II,III)-silicate phases (Fig. 3b, 4). These ores have a massive texture and occur as thin, parallel, or wavy laminae. The northwest ore belt is mainly black shale, with ore beds containing Mn-carbonate (Fig. 3b, 4). The most remarkable features of these Mn carbonate ores are the nodules, oolites, and spherulite textures. The lateral lithological change in the host rock from reddish-brown mudstone to black shale may indicate a transition to a deeper-water depositional environment to the northwest. In addition, supergene oxidized ore zones are distributed in both the SE and NW belts. These altered zones mainly contain pyrolusite (MnO_2) (Fig. 3b).

3. Materials and Methods

Samples of primary Mn ores were collected from underground tunnels in active Mn mines (41.019ºN, 120.143ºE). This allowed for larger samples of fresh material to be collected. Samples are unlikely to have experienced extensive weathering or meteoric alteration prior to collection as they have only recently been exposed during mining operations. Areas where supergene alteration has resulted in zones of oxidized ore were avoided during sampling.

Fourteen hand samples were obtained from the SE ore belt (samples no. SE-1 to -14), capturing the entirety of the three ore beds. From the NW ore belt, six samples (NW-1 to -6) were collected only from the lower and middle ore beds, as the upper ore bed has been exposed at the surface. A total of twenty blocks (5cm x 3 cm x 5 cm) were subsampled from hand samples after any exposed surfaces were removed. These blocks were then cut into two equal parts along the vertical dimension. The two slabs were used for further analysis by a range of methods as either polished thin sections or milled powders. Petrographic features were imaged by backscattered electron (BSE) microscopy, and images of carbon-coated samples were acquired on a JEOL JXA-8100 scanning electron microscope (SEM) at the Laboratory of Microscopy and Microanalysis, Wuhan Microbeam Analysis Technology Co. Ltd. SEM-energy dispersive X-ray spectrometry (EDS) was subsequently used to qualitatively identify and map Mn-bearing minerals.

3.1 Laser Raman spectroscopy

Mineral compositions were quantified using a Renishaw RM1000 laser Raman spectroscopic instrument housed at the State Key Laboratory of Geological Processes and Mineral Resources (GPMR), China University of Geosciences (Wuhan). The laser was argon sourced with a wavelength of 514.5 nm and a source power of 5 mW. The charge-coupled device (CCD) detector had an area of 20 μm^2. The spectra were recorded with counting time of 30 s over a range from 100 to 1400 cm^{-1}. A spectrograph aperture of 25 μm was chosen for the analysis. Instrumental settings were kept constant across all analyses (Table S1). Raman standard spectra were acquired from the RRUFF Project website (https://rruff.info/).

3.2 X-ray photoelectron spectroscopy

X-ray photoelectron spectroscopy (XPS) measurements were performed at the Wuhan Shiyanjia Laboratory using an ESCALAB 250Xi spectrometer with a monochromatic Al Ka X-ray (1486.6 eV) source operating at 16 mA and 12.5 kV. All sample preparation occurred under atmospheric conditions. Collection efficiency was enhanced by performing 10 cycles of signal accumulation. Mn2p, Mn3p and Fe2p lines were measured using a 400 mm spot size. Survey scans were recorded using a fixed pass energy (PE) of 100 eV and a step size of 0.5 eV, whereas narrow scans were collected using a fixed PE of 30 eV with a step size of 0.05 eV. Samples analyzed were charge referenced to the carbon C1s peak at 284.80 eV. Spectra were best fit, after Shirley background subtractions, by linear least squares using the Advantage software package (Table S2).

3.3 Inorganic carbon isotope analysis

Inorganic carbon isotopic compositions were measured on bulk Mn carbonate ore samples using a Thermo Finnigan Delta V Plus continuous flow isotope ratio mass spectrometer (IRMS) at the State Key Laboratory for Mineral Deposits Research of Nanjing University, China. Approximately 100 μg of sample powder was dissolved using orthophosphoric acid at 70 °C for >24 h in a continuous flow sample preparation device connected to the IRMS. All isotopic ratios are expressed as per mil relative to the Vienna Peedee Belemnite (V-PDB) standard. The internal precision (1SD) was less than ±0.1‰ for $\delta^{13}C$ values, and the external precision was better than ±0.5‰ for $\delta^{13}C$ values.

3.4 Total organic carbon

For TOC measurements, samples were leached with excess ~20% hydrochloric acid to remove carbonate phases and washed in distilled water prior to analysis at the State Key Laboratory of Geological Processes and Mineral Resources (GPMR), China University of Geosciences (Wuhan). The dried residue and non-acidified samples were measured using either a Jena Eltra 4000 carbon-sulfur analyzer or Beijing Wanlianda-Kexin CS-902 high-frequency infrared ray carbon-sulfur analyzer for TOC and total carbon (TC) contents, respectively. Total inorganic carbon (TIC) contents were calculated by the difference between TC and TOC values. Analytical quality was monitored based on repeated analysis of Alpha Resources standard AR 4007 (TC = 7.27%) with an analytical precision better than 0.2%.

3.5 Major element analysis

Major elements, reported as oxides (Al_2O_3, CaO, TFe_2O_3, K_2O, MgO, MnO, Na_2O, P_2O_5, SiO_2, TiO_2, and LOI), were analyzed on bulk rock samples at Yanduzhongshi Geological Analysis Laboratories Limited. Fresh samples were first broken into centimeter-sized pieces. Fresh pieces were then washed with deionized water, dried, and ground to less than 200 mesh (0.5200 ± 0.0001 g) for geochemical analyses. Sample powders were fluxed with $Li_2B_4O_7$ (1:8) to make homogeneous glass disks at 1250 °C using a V8C automatic fusion machine produced by the Analymate Company in China. Bulk rock major elements were analyzed using X-ray fluorescence spectrometry techniques (Zetium, PANalytical or XRF-1800, Shimadzu). Analytical errors for major elements are estimated to be less than 1%. Information on standards (National Standard, GB/T 14506.30-2010) and precision can be found in Table S3.

4. Results

4.1 Petrography

Mudstone and shale wall rocks (sample SE-1 and NW-1) in the SE and NW ore belts, respectively, are mostly composed of detrital quartz and clay minerals (Fig. 5). The difference between these two belts, however, is manifested in the degree of rounding, the size of quartz grains, and clay mineral content. Additionally, only the SE ore belt contains detrital feldspar (Fig. 5a).

4.1.1 The Southeast ore belt

Laser Raman spectroscopy (Fig. S1) indicates that the minerals in the SE ore belt are characterized by partially oxidized phases including Mn(II,III)-oxides [hausmannite (Mn_3O_4), manganite (MnOOH)] and -silicate [braunite ($Mn(III)_6Mn(II)O_8SiO_4$)], Mn(II)-carbonate [Ca-rhodochrosite $Mn(Ca)CO_3$], and hematite [$Fe(III)_2O_3$]. Mn(II)-carbonate and braunite are the main mineral phases in the lower ore bed (Fig. 6a, 7b, 8e, 9c). In samples SE-2 and -7 (Fig. 6a, 10a), Mn(II) carbonate is present as a cement that solidifies sub-rounded to sub-angular quartz grains and is concentrated in residual pore space. Scarce hausmannite in sample SE-4 displays a representative contact where it has been replaced, or crosscut, by braunite (Fig. 8b). Hausmannite is destroyed and closely associated with Mn(II) carbonate (Fig. 8c, e, f). Remarkably, we note the presence of hausmannite and braunite as inclusions, or unreacted residues, trapped within Mn(II) carbonate (Fig. 8d). Further, in sample SE-5 (Fig. 9a, b), Ca-rhodochrosite has destroyed the subhedral habit of braunite, where it appears to have replaced braunite grains. Moreover, Ca-rhodochrosite occurs along the rim of the braunite grains. In sample SE-6 (Fig. 9c, d), hausmannite is also observed as disseminated inclusions within a Mn(II) carbonate assemblage.

A large component of hematite is observed, and it is closely associated with Mn(II) carbonate in the lower ore body. Hematite is documented in several textural contexts, including; (1) spheroidal hematite clusters in Mn(II) carbonate nodules (Fig. 6b-d), (2) grains with concentric rings of hematite and Mn(II) carbonate (Fig. 7), and (3) hematite with Mn(II) carbonate along the rim of detrital quartz and feldspar (Fig. 10c). Similar structures also appear in the layer between the middle and lower ore bed as observed in SE-8 (Fig. 11).

The middle ore bed is devoid of Mn(II,III) silicate and Mn(II) carbonate, however, manganite is present (Fig. 12a, b). Manganite, with some Fe content, is also present in the interval where detrital minerals are most abundant (Fig. 12c and mapping). In addition, hematite occurs in the middle ore bed and presents a clear paragenetic relationship with manganite (Fig. 13a-c) rather than the Ca-rhodochrosite described in the lower ore bed. In Fig. 13a, a mixed oxide phase with both Mn and Fe content is observed in close association with hematite and manganite minerals.

In the upper ore bed there is a lack of Ca-rhodochrosite. However, braunite and manganite are observed with evident replacement textures (Fig. 14). Notably, some braunite appears to have replaced manganite, but this appears to be patchy and incomplete, with relict manganite observed (Fig. 14b, c and mapping). Hematite or other Fe-containing minerals phases are not present, or are rare, within the upper ore bed.

4.1.2 The Northwest ore belt

In contrast to the common oxidized mineral phases observed in samples from the SE ore belt, Ca-rhodochrosite is ubiquitous in the NW ore belt. This results in the NW ore belt presenting a more reduced mineralogy than the SE ore belt. Further, while the Mn(II) carbonate is ubiquitous, the main component of the matrix in the NW ore belt is quartz (Fig. 5b).

In the lower ore bed, nodules and oolites (with diameters > 100 μm and composed of Ca-rhodochrosite) phases are characteristic and widespread (Fig. 15a, b). The interior of these nodules commonly displays a banded structure with concentric rings (Fig. 15c-e). The different colored rings (grey and darker grey) correlate with differences in the Mn (Ca):Fe (Mg) ratio within Mn-Fe carbonate phases (Fig. 15d). This is corroborated by EDS analyses. Similar oolitic structures, ~10 μm in diameter, are present in the middle ore bed (Fig. 16a, b). Additionally, in the massive ore present in the upper bed (Fig. 16c), several residual magnetite and Mn-Fe carbonate grains occur as a replacement assemblage (Fig. 16d-f).

BSE images show that abundant, randomly oriented platy particles, that are variable in size, are enclosed in quartz. These sub-micron-sized particles display face-to-face and face-to-edge ("cardhouse") contacts (Fig. 16g-i). Raman data indicate that these plates are chamosite [$Al_2Fe(II,III)_5(OH)_8O(SiO_3)_3$] and contain some residual organic matter (Fig. S1).

4.2 Speciation of Mn and Fe

The redox state of Mn and Fe were determined by XPS Mn2p, Mn3s and Fe2p analyses. The quantitative curve fit results for XPS spectra are illustrated in Table 1. Fit results of the Mn2p and Mn3s spectra from the SE samples indicate that the Mn valence is more varied than that of the NW belt which is characterized dominantly by reduced Mn(II)-carbonates. In other words, for the NW belt, the valency of Mn is generally +2. In the SE ore belt, however, the dominant Mn valence state differs between the lower, middle, and upper ore beds. The Ca-rhodochrosite in the lower bed and some manganite samples in the middle bed are reflected by signals that correspond to Mn(II) and Mn(III), respectively. The Mn XPS spectra of the samples from the lower and upper beds with various Mn-mineral phases can be determined based on the observed peaks, and indicate that Mn is present in mixed valence phases, in varying proportions of Mn(II) and Mn(III). Notably, in addition to the Mn(III) signal observed, some manganite samples in the middle bed also contains detectable Mn(IV). All Fe-containing ore beds in SE belts contain Fe(III), while Fe(II) is observed in the Mn-Fe carbonate sample from the lower ore bed. Similarly, Fe(II) is present in middle ore bed samples in the NW belt that are composed of chamosite and magnetite.

4.3 Geochemical data

Differences in the content of Mn and Fe, $\delta^{13}C_{carb}$ values, and total organic carbon (TOC) content exist between the SE and NW ore belts (Fig. 4, Table 2). The SE belt is characterized by higher Mn content (generally > 30 wt%), generally less Fe content (< 7 wt%), and higher Mn/Fe (up to 18) and Fe/Al (up to 14) ratios. The NW belt, on the other hand, is characterized by ~25 wt% Mn, 12 wt% Fe, and Mn/Fe ratios of ~2 and Fe/Al value of ~1.1 to 6.2. All Fe/Al ratios are higher than the average Tieling shale. While all $\delta^{13}C_{carb}$ values are isotopically light (-7‰ to -4‰), the NW belt is characterized by samples with a more depleted isotopic composition. In addition, relative to the NW belt (~ 0.9%), the SE belt is scarce with respect to TOC (< 0.2%).

5. Discussion

5.1 Manganese cycling

5.1.1 Mn(III,IV) oxide constraints on redox conditions

Manganese is a strongly redox-dependent element in aqueous systems (e.g., Johnson et al. 2016a). Under reducing conditions, Mn tends to exist as soluble Mn(II), while in oxic environments it commonly occurs as the relatively insoluble Mn(III,IV)-oxyhydroxides or -oxides (Trobovillard et al. 2006). Due to the relatively high redox potential of $Mn(IV)O_2/Mn(II)$ (+1.23 V; Lide 2004), the oxidation of Mn(II) is typically considered to require higher redox potentials generated by the presence of free dissolved oxygen at concentrations >10 μM (e.g., Planavsky et al. 2014a; Tostevin et al. 2016; Ossa et al. 2018; Lingappa et al. 2019). Moreover, given strong kinetic limitations, Mn(II) oxidation is considered to be typically catalyzed by either microbial activity through direct enzymatic activity (Tebo et al. 2005), or by metal oxide surfaces coupled to the reduction of O_2 or O_2-derived species such as superoxide (Morgan 2005; Hansel et al. 2012).

Based on an earlier hypothesis of direct photosynthetic Mn(II) oxidation (Olson, 1970; Johnson et al. 2013), recent experiments have shown the potential for the oxidation of Mn(II) in anoxic aqueous solutions by anoxygenic phototrophs (Daye et al. 2019) or through photochemical oxidation by ultraviolet light (Anbar and Holland 1992; Liu et al. 2020b). Incubation experiments show that the initiation of Mn redox cycling only requires very low dissolved O_2 concentrations ($[O_2] < 0.5$ μM; Schippers et al. 2005). Although plausible, these processes are inhibited by the presence of reductants (e.g., Fe(II); Planavsky et al. 2014a). To this end, the presence of appreciable Fe(II) under anoxic conditions will lead to the reduction of Mn(IV) oxides within the water column, preventing substantial Mn from accumulating in sediments. Furthermore, the low rates of these processes make them unlikely to be geologically significant (e.g., Lyons et al. 2020). In this regard, primary or early formed Mn (III,IV) oxides can be considered as sensitive indicators of the redox state and may be used to reconstruct the oxidation state of the ocean-atmosphere system contemporaneous to deposition (Robbins et al. 2023 for a review).

5.1.2 Mn(III) and paragenetic pathways

It is generally accepted that the primary Mn phases delivered to the sediment pile from oxic seawater are Mn(IV) oxides, rather than Mn(III)-bearing oxides such as feitknechtite (MnOOH) (Calvert and Pedersen 1996; Tebo et al. 2005; Planavsky et al. 2021), as the oxidation of Mn(II) by O_2 via the transfer of a single electron has been demonstrated to be thermodynamically unfavorable (Bargar et al. 2000, 2005; Luther 2010). Yet, insoluble Mn(III)-oxide phases may form through the reductive transformation of Mn(IV) to Mn(II) by metal-reducing bacteria (e.g., Lin et al. 2012) and may be important intermediate phases in the sedimentary redox cycling of Mn. Alternatively, Mn(III)-oxyhydroxides could form when dissolved Mn(II) is oxidized by $Mn(IV)O_2$ in porewaters (Bargar et al. 2005; Elzinga 2011; Madison et al. 2013; Johnson et al. 2016b; Oldham et al. 2017):

$$Mn(II) + Mn(IV)O_2 + 2H_2O \rightarrow 2Mn(III)OOH + 2H^+ \qquad (1)$$

Importantly, metastable Mn(III) oxyhydroxide (e.g., feitknechtite) is a solid phase that could potentially enter the sedimentary record and subsequently form either manganite at pH 7.0-7.5 or hausmannite at pH > 8.0 (e.g., Lefkowitz et al. 2013; Elzinga and Kustka 2015). Recent work on bacterial Mn(II) oxidation has demonstrated that soluble Mn(III)-ligand complexes (e.g., pyrophosphate or siderophores) occur as short-lived intermediates during the oxidation of Mn(II) to Mn(IV)-oxide (Webb et al. 2005; Parker et al. 2007; Learman et al. 2011). However, it is not common to observe substantial accumulations of Mn(III) phases because they are subsequently fully oxidized to Mn(IV) oxides.

On the whole, Mn(III) minerals likely represent important intermediary phases that reflect the reduction of Mn(IV) to Mn(II) during the transition from oxic to anoxic conditions (Tsikos et al. 2003; Johnson et al. 2016b). Therefore, the accumulation of appreciable Mn(III,IV) oxides or Mn(III)-bearing mineral phases in the geologic record should be considered to reflect first-order changes in the availability of O_2 and oxidizing paleoenvironmental redox conditions.

5.1.3 The redox-indicator significance of Mn(II) mineral phases

While primary Mn(III,IV) oxides can be used as “oxidation-sensitive mineral indicators”, most ancient Mn deposits consist primarily of Mn(II) minerals (either as Mn(II)-carbonates or -silicates). Traditional models for Mn deposits assume that the overlying waters were oxygenated to some degree and that the primary Mn minerals were Mn(IV) oxides (e.g., Maynard 2010; Johnson et al. 2016a; Yan et al. 2022); in this sense their formation is similar to that proposed for many Fe formations (e.g., Konhauser et al. 2017). Given this view, the reduced Mn(II) mineral phases that are present in the sedimentary rock record are regarded as diagenetic products generated by biological reduction of Mn(IV) oxide through dissimilatory Mn reduction (DMR) coupled to the oxidation of organic matter (e.g., Maynard 2010), or abiotic reaction (AR) via oxidation of sulfides (H_2S or pyrite) or Mn/Fe(II) (e.g., Van Cappellen et al. 1998; Johnson et al. 2016a).

Alternatively, it has been proposed that Mn(II)-carbonate phases can directly accumulate in sediments below anoxic bottom waters following nucleation on biogenic calcite in an oxygen-minimum zone as calcite may trigger Mn(II)-carbonate precipitation (Farquhar et al. 2014; Herndon et al. 2018; Siahi et al. 2020; Wittkop et al. 2020; Gao et al. 2021; Chen et al. 2022). Similarly, Mn(II)-silicates may form through the primary accumulation of an amorphous Mn(II)-Si gel under anoxic conditions before undergoing post-depositional transformations (Flohr and Huebner 1992; Manceau and Gallup 2005; Brusnitsyn 2006; Brusnitsyn et al. 2017). None of these proposed mechanisms require Mn(IV)-oxides to be present as the primary minerals and thus, they decouple the formation of appreciable sedimentary Mn deposits from an oxidative mechanism. In instances where small amounts of Mn(IV)-oxides were reported, they were often attributed to the oxidation of Mn(II)-carbonate and -silicate minerals by meteoric fluids or the atmosphere following exposure at the surface (e.g., Johnson et al. 2016a). In such a case, the presence of Mn(IV)-oxides would reflect a weathering signal rather than a reliable proxy for paleoenvironmental redox conditions. While the unique geochemical properties of Mn impart a potentially important role for sedimentary Mn deposits at indicating the redox evolution of ancient marine settings, it is critical that the Mn mineral assemblage, paragenetic sequence, and formation mechanism(s) of precursor phases are accurately constrained.

5.2 Mineral paragenesis

$\delta^{13}C$ values provide an important line of evidence for explaining the origin of Mn(II)-carbonate in the ore belts (e.g., Maynard 2010). For example, in the model where Mn(II) oxidation in the water column results in the deposition of Mn(IV)-oxides, the Mn(II)-carbonate is thus a secondary mineral formed via DMR. As such, it should be characterized by more depleted $\delta^{13}C_{carb}$ values than those of the contemporaneous seawater because the carbonate is derived from biomass enriched in ^{12}C. Conversely, when Mn(II)-carbonates result from the direct combination of Mn(II) and inorganic carbon from seawater, the $\delta^{13}C_{carb}$ values should reflect that of contemporaneous seawater. Although isotopically light $\delta^{13}C_{carb}$ values in sediments may also result from sulfate reduction coupled to organic matter oxidation (e.g., Hausler et al. 2018), low seawater sulfate contents during mid-Proterozoic and a lack of sulfide species (pyrite) in the Wafangzi Mn carbonate indicates that sulfate reduction was limited in this area.

Mesoproterozoic strata from the North China platform have $\delta^{13}C_{carb}$ values close to 0‰ and do not display a significant gradient in $\delta^{13}C_{carb}$ from shallow- to deep-water settings (Guo et al. 2013; Luo et al. 2014; Yu et al. 2022). Therefore, the light $\delta^{13}C_{carb}$ values of the Wafangzi Ca-rhodochrosite suggests that they were not formed in isotope equilibrium with seawater and thus are not direct seawater precipitates. The depleted $\delta^{13}C_{carb}$ values instead suggest that the Ca-rhodochrosite formed because of organic matter respiration which resulted in elevated HCO_3^- concentrations and alkaline pH conditions. These conditions can be met in anoxic porewaters during diagenesis and DMR, thus generating supersaturation with regards to Ca-rhodochrosite. As marine sedimentary porewaters are typically Ca-rich (~10.5 mM), precipitation of carbonates generally results in the formation Mn-Ca carbonates (e.g., Ca-rhodochrosite) – that we observe in our sediments - rather than a pure rhodochrosite ($MnCO_3$) endmember when there is sufficient Mn(II) (Brand and Veizer 1980; Neumann et al. 2002; Mucci 2004).

Petrographic observations also discount a direct seawater Mn(II) carbonate precipitation pathway as one would expect fine-grained calcite crystals surrounded by Mn(II) carbonates, similar to the features observed in primary Mn(II) carbonate deposits (e.g., Wittkop et al. 2020; Gao et al. 2021; Chen et al. 2022). Such features, however, are lacking in our samples. By contrast, we interpret many Ca-rhodochrosite nodules with concentric rings, which are ubiquitous in the NW belt, to reflect a diagenetic banded structure (Fig. 15, 16a, b). Similar microstructures are common to Carboniferous Mn(Ca)-carbonate deposits, Northwest China, that have been proposed to reflect microbial Mn(IV) oxide reduction and the active release of Mn(II), followed by Ca-rhodochrosite nucleation on microbial surfaces (e.g., Huang et al. 2022).

The relationship between Mn(III) mineral phases (hausmannite, braunite) and Mn(II) carbonate (Ca-rhodochrosite) in our samples is suggestive of a replacement texture and may help further constrain the Mn mineralization mechanism (Fig. 8, 9). When compared to characteristic petrographic structures for Mn(III,IV)-oxides, such as inclusions in Mn(II) carbonate nodules or the replacement of Mn(III,IV)-oxides by Mn(II)-carbonate (e.g., Johnson et al. 2016a; Yan et al. 2022), the Mn(III) mineral phases from the lower bed of the SW belt are more consistent with an early formed oxidized phase preserved as an unreactive residue, rather than a product of secondary oxidation of Mn(II). Further, the hausmannite and braunite in our samples both appear as a hard, mineralized texture, as opposed to a weathering product which generally produces Mn(IV)-oxides that have “fibrous” morphologies (Johnson et al. 2016a). Additionally, the spatial replacement relationship between these two Mn(III) mineral phases indicate that hausmannite was formed earlier than braunite (Fig. 8b).

Another Mn(III) mineral phase, manganite, is observed as an intergranular cement, infilling the secondary pore space between detrital grains (Fig. 12c). This relationship indicates that the manganite postdates deposition, but formed prior to compaction during diagenesis, otherwise the pore space would have been occluded, which is similar with diagenetic hematitic cement in the intergranular pore space within oxidized red beds (e.g., Matheson and Pufahl 2021). In addition, the observation that euhedral to subhedral manganite was replaced by braunite suggest that the manganite formed earlier during diagenetic processes (Fig. 14b, c). Based on the petrographic relationships observed here, it is unclear whether hausmannite and manganite were coeval, or if one was derived from the other. From a purely stochiometric view, the average Mn valence of manganite (~3) should be higher than that of hausmannite (~2.6). Analysis of XPS data, however, indicated that while Mn(IV) is present in the massive manganite rocks, it is conspicuously absent in the hausmannite-bearing rocks (e.g., SE-6). Assuming that Mn(IV)-oxides were the primary phase, this would suggest that manganite is the earliest preserved mineral phase in our samples. On the whole, even though Mn(IV)O_2 is not observed in our samples, the Mn(III) mineral phases in the SW belt are most parsimoniously explained as an intermediate product resulting from the reduction of primary Mn(IV)O_2 during early diagenesis as DMR leads to the formation of rhodochrosite. Given the petrographic relationships noted here, the paragenetic sequence from earliest to latest formed, is suggested to be: manganite, hausmannite, braunite, and finally Ca-rhodochrosite.

Hematite, with a variety of structures, is ubiquitous in SE belt. The origin of hematite in sedimentary rocks has long been interpreted to be the results of: (1) the dehydration of colloidal Fe(III)-oxyhydroxide particles formed in oxic water column, as in the prevailing depositional model for BIFs (e.g., Sun et al. 2015; Konhauser et al. 2017); (2) an early-diagenetic authigenic product generated through the oxidation Fe(II) by oxic porewaters or an oxidant in the sediment pile, such as for hematite coatings on quartz grains observed in red beds (e.g., Matheson and Pufahl 2021); or (3) the post-depositional oxidation of Fe(II) minerals such as greenalite precipitated out of an anoxic water column (e.g., Rasmussen et al. 2014). X-ray photoelectron spectroscopy and petrographic observations indicate that the hematite is characterized solely by Fe(III) in samples from the SE ore belt, as would be expected. The lack of a residual Fe(II) valence state suggests that the hematite is unlikely to be derived from post-depositional oxidation of reduced Fe mineral phases. Further, it is difficult to imagine post-depositional processes that would have oxidized only the Fe(II), and not Mn(II), given their close association. In general, the hematite, which was likely derived from a precursor Fe(III)-oxyhydroxide phase that precipitated as loosely bound floccules in the water column, appears to be randomly oriented in the matrix rather than being concentrated in the residual pore space (e.g., Rasmussen et al. 2017; Tang et al. 2020). However, the hematite in sample SE-7 and -8 filling in the interval of detrital grains supports a diagenetic origin (Fig. 10, 11). Previous studies have proposed that during Mn-Fe cycling in marine redox stratification systems, Mn(IV)O_2 would be an oxidant for dissolved Fe(II) or iron sulfide [pyrite; Fe(II)S_2], leading to the formation of Fe(III)-oxyhydroxides and reduced Mn(II,III) phases or the return of Mn(II) to the water column (Dellwig et al. 2010; Maynard 2010).

The paragenetic sequence with respect to the Mn mineral phases may also provide important evidence for constraining the formation of hematite in these samples (Fig. 6, 7, 11, 13b, c). For instance, reactions 2-5 could have led to Mn(IV)O_2 reduction and the simultaneous oxidation of Fe(II) phases during diagenesis, generating reduced Mn minerals and hematite (via alteration of a ferrihydrite precursor).

$$2MnO_2 + 2Fe(II) + 3H_2O \rightarrow 2MnOOH + Fe_2O_3 + 4H^+ \quad (2)$$

$$30MnO_2 + 2FeS_2 + 11H_2O + 8OH^- \rightarrow 30MnOOH + Fe_2O_3 + 4SO_4^{2-} \quad (3)$$

$$3MnO_2 + 2Fe(II) + CH_2O \rightarrow MnCO_3 + Fe_2O_3 + 2Mn(II) + H_2O \quad (4)$$

$$17MnO_2 + 2FeS_2 + CH_2O + 24H^+ \rightarrow MnCO_3 + Fe_2O_3 + 16Mn(II) + 4SO_4^{2-} + 13H_2O \ (5)$$

The paragenesis of Mn phases may ultimately reflect the relative abundance of reductants, including detrital pyrite, dissolved Fe(II) and organic matter, which would induce the reduction of Mn(IV) oxides. Beacuse low sulfate concentrations in the mid-Proterozoic seawater inhibited the widespread precipitation of pyrite, instead, most of the Fe(II) was likely associated with Fe(II)-carbonate and -silicate in Wafangzi deposit. The conspicuous absence of pyrite in adjacent wall rock samples from the region (Fig. 4) may also exclude the possibility that detrital pyrite was transported to Mn ores. In addition, in several samples, the surrounding detrital clay minerals with little Fe content (Fig. 5a) exclude the detrital dissolved Fe(II) source, but indicating interactions with Fe(II)-rich porewaters. Ferruginous conditions were both spatially and temporally extensive in marine settings throughout the mid-Proterozoic (e.g., Planavsky et al. 2011; Poulton and Canfield 2011), consistent with the high Fe/Al ratios from our samples.

Thus, Fe(II) diffused from ferruginous porewaters or seawater in the upper sediment pile may have created conditions where Fe(II) acted as a reductant for Mn(IV)O_2 and was oxidized to form hematite during early diagenesis.

Dissimilatory iron reduction (DIR) – where iron-reducing bacteria utilize Fe(III)-oxyhydroxides as terminal electron acceptors during organic matter oxidation (Konhauser et al. 2005) – leads to increased alkalinity (e.g., HCO_3^-), which when in the presence of dissolved Mn(II), would lead to Ca-rhodochrosite precipitation. To this end, the concentric ring structures observed (Fig. 15c-d, 16a-c) may be attributable to cyclical changes in the Mn/Fe of porewaters due to fluctuations in the generation of Mn(II) by DMR. However, the formation of Fe-bearing mineral phases during early diagenesis through DIR can also not be discounted. Indeed, a small number of reacted, residual magnetite (Fe_3O_4) grains are observed in the Mn(Fe)-carbonate (Fig. 16d-f). This magnetite would likely have formed through the interaction of Fe(III)-oxyhydroxides with dissolved Fe(II) and/or organic matter during diagenesis and metamorphism (Li et al. 2013; Halama et al. 2016). The required precursor Fe(III)-oxyhydroxides could signify original Fe(II) oxidation by iron-oxidizing photosynthesis, or more likely for the mid-Proterozoic, interactions with oxygen in water column (Schad et al. 2019). Another line of evidence for primary Fe(III) arises from the abundant chamosite with mixed Fe(II) and Fe(III) that is present in the NE belt (Table 1).

Various mechanisms have been proposed to account for the presence of Fe(II,III) silicates. First, either all, or at least a small proportion of, aqueous Fe(II) in the water column is oxidized to form an initial Fe(III)-oxyhydroxide or metastable Fe(II,III) precursor phase such as green rust [$Fe(II)_3Fe(III)(OH)^{8+}$•Cl•nH_2O] (e.g., Li et al. 2017; Halevy et al. 2017; Johnson et al. 2018; Nims and Johnson 2022). This is followed by the adsorption of silica during settling through the water column and/or in the sediment porewater, which would have induced the transformation of these Fe(III) phases into thermodynamically more favorable Fe(III)-bearing silicates (e.g., Phoenix et al. 2003). Next, a net chemical reduction of these Fe(III) silicates could occur during descent of the particles through the ferruginous water column or in pore waters if reductants are present, resulting in an increase in the Fe(II) content of the mineral. Alternatively, the existence of Fe(III) in Fe(II) silicate could be as a result of structural Fe(II) oxidation from secondary fluids during post-lithification (Rasmussen et al. 2014).

In our samples, chamosite aggregates in quartz resemble partial floccules in clay slurries of freshly deposited, modern marine muds (Nishida et al. 2013; Deirieh et al. 2018), which suggest that the chamosite precursor was an Fe(III)-bearing phase, rather than subsequent post-depositional oxidation (Fig. 16g-i). Similar textures defined as primary sediments have been also described in BIF where randomly oriented, Fe(III)-bearing greenalite particles are enclosed in chert (Rasmussen et al. 2017; Johnson et al. 2018). In addition, the finding of residual organic matter (Fig. S1) suggests that the partial reduction of an Fe(III) precursor by DIR occurred in the porewaters, forming mixed valence Fe minerals which were later altered to chamosite under elevated concentrations of Si and Al.

5.3 Mineralization model of Wafangzi Mn deposit

Observations on textural and mineralogical associations, carbon isotope compositions, and Mn-Fe redox conditions presented here constrain the precipitation and mineralization of the Wafangzi Mn deposit. Deposition likely occurred through the oxidation of Mn(II) in a redox-stratified water column, where a manganous water layer may have existed between shallow oxygenated water and deeper ferruginous waters (Fig. 17). Following the oxidation of Mn(II) that was upwelled from deeper anoxic waters, primary Mn(IV)-oxides precipitated when they encountered overlying oxic shallow seawater. Contemporaneously, the precipitation of Fe(III)-(oxyhydr)oxide may have started under lower oxygen or anoxic conditions, potentially via photoferrotrophy in waters directly overlying deeper anoxic ferruginous waters, but still within the photic zone (e.g., Konhauser et al. 2002). As Fe(II) oxidation would have been progressive during upwelling as anoxygenic photoferrotrophy may exist deeper within the water column proximal to redoxclines (e.g., Kappler et al. 2005; Jones et al. 2015), Fe concentrations would likely have decreased as water depth shallowed through the Mn redoxcline into shallow and locally oxygenated waters (e.g., Smith and Beukes 2023). Thus the elevated Mn/Fe and decreased Fe/Al ratios from the deeper NW to shallower SE belt may reflect the progressive removal of dissolved Fe(II) from seawater and enhanced precipitation of Mn-oxides in more oxygenated settings. A similar mechanism has been proposed for Mn enrichments in the ~2.95 Ga Ijzermign Iron Formation in South Africa (Smith and Beukes 2023) where Fe(II) is progressively removed in deeper waters allowing for Mn oxidation and accumulation in shallower, more proximal settings. This would also explain the characteristics Fe(II) oxidation and water column precipitation that occurred solely in the deeper NW belt, while the shallower SE belt captures Fe textures more indicative of porewater processes.

Here, we have defined "Mn-redoxcline" in a broader sense than a dashed line typically shown in many papers (e.g., Maynard 2010). Maintaining a vigorous oxidation of Mn requires higher oxygen concentrations ($[O_2] > 10$ μM). Here, we define a "manganous zone" with 0 to 10 μM O_2 where there is an abundance of Mn(II). In this sense, the "manganous zone" may be considered as analogous to a "suboxic zone" between oxygenated surface and anoxic (ferruginous) bottom waters. However, the initiation of Mn(II) oxidation requires only low dissolved O_2 concentrations ($[O_2] \sim 0.5$ μM; Schippers et al. 2005). Additionally, most of the precipitated Mn(IV)-oxides progressively, rather than immediately, redissolve as they settle downwards through a suboxic water column. Once in the anoxic zone, particulate Mn(IV)-oxides may be completely dissolved in the water column. Thus, appreciable Mn(IV)-oxide may be present in the "suboxic zone", which justifies the broader definition of "Mn-redoxcline" used here.

During early diagenesis in the sediment pile, Mn(IV)-oxides were reduced by organic matter (DMR) or Mn/Fe(II) (AR), resulting in the formation of the Mn(III) mineral phase (e.g., manganite) with some ferrihydrite. The manganite then transformed to Mn(II,III)-oxides (e.g., hausmannite), or combined with silica to form Mn(II,III)-silicates (e.g., braunite). Meanwhile, ferrihydrite settled to the seafloor where it was during burial converted to mixed ferrous/ferric phases, such as green rust, before their final transformation to magnetite and chamosite. Where there was excess ferrihydrite relative to organic carbon, the ferrihydrite would instead have transformed into hematite (Konhauser et al. 2005). For Fe minerals, this is especially prevalent in the NW belt. Finally, Mn(II)-Fe(II) carbonates were formed through the continued reduction of precursor phases during subsequent diagenesis.

Our observations indicate that for the Wafangzi Mn deposit there is a general pattern with regards to the distribution of Mn(II) carbonates in the NW belt and Mn(III) and Mn(II) phases in the SE belt. However, the controls on the distribution of these assemblages remains unconstrained. As discussed above, decomposition of organic matter via DMR is likely the main process driving Mn(IV) reduction for large sedimentary Mn enrichments. Microbially mediated DMR may proceed via reaction 6:

$$2MnO_2 + CH_2O + HCO_3^- \rightarrow 2MnCO_3 + OH^- + H_2O \qquad (6)$$

Where 1/2 of carbon is generated through the decomposition of organic matter by DMR, with the remainder coming from bicarbonate from either coeval seawater or porewaters. In this case, assuming that the $\delta^{13}C$ composition of Mesoproterozoic organic matter is close to −30‰ ($\delta^{13}C_{org}$) and the $\delta^{13}C$ of seawater HCO_3^- is close to 0‰ (Yu et al. 2022), the $\delta^{13}C_{carb}$ of rhodochrosite generated during early diagenesis would be expected to be ~ −15‰. Even if DIR that formed Fe(II)-carbonate by reaction 7 diluted the signal, the $\delta^{13}C_{carb}$ signal would be just expected to trend to slightly higher values (~ −7.5‰).

$$4Fe(OH)_3 + CH_2O + 3HCO_3^- \rightarrow 4FeCO_3 + 3OH^- + 7H_2O \qquad (7)$$

Thus, the higher $\delta^{13}C_{carb}$ values (> -7‰) observed in the SE and NW ore belts may indicate the influence of reductants such as porewater Fe(II) or Mn(II), in addition to organic carbon. In this regard, the relatively more depleted $\delta^{13}C$ values in samples from the NW ore belt, where only Mn(II)/Fe(II)-carbonate is observed, may represent more proportion of organic matter burial, relative to the SW ore belt. If organic carbon fluxes were greater than that of Mn(IV)-oxides, then quantitative Mn(IV)-oxide reduction may have occurred. Conversely, a greater flux of Mn(IV), relative to organic matter, would have resulted in partial Mn(IV)-oxide reduction and more oxidized phases being preserved. The relative degree of fluxes would have similar implication for the development of the iron mineral assemblages. Thus, the obvious difference in the paragenetic assemblage of Mn and Fe minerals between the NW and SE ore belts may be best interpreted as reflecting differences in the degree of organic matter delivery. This would be consistent with the high TOC content of samples from the NW belt, where greater organic carbon fluxes were likely involved in the principal sediments during initial deposition. This may have been the result of the NW ore belt occupying a deeper sedimentary position with limited oxygen in the overlying waters, which would have inhibited organic matter consumption during sinking through the water column.

6. Implications

The mid-Proterozoic has historically been interpreted to represent an interval of relative stability across the Earth's biogeochemical cycles, even being referred to as the 'Boring Billion' (e.g., Brasier and Lindsay 1998) and dominated by persistent anoxia (e.g., Reinhard et al. 2013; Planavsky et al. 2014b; Cole et al. 2016). This period is generally considered to have been characterized by atmospheric oxygen levels of <0.1–1% PAL (present atmosphere level) and dominantly anoxic ferruginous seawater with euxinic waters variably developed at productive continental margins (e.g., Planavsky et al. 2011; Poulton and Canfield 2011; Tang et al. 2017). However, an increasing number of studies from globally-distributed marine basins suggests that there were several pulsed episodes of oxygenation events that occurred during the mid-Proterozoic, which resulted in transient periods of elevated atmospheric O_2 levels that may have reached ~1–10% PAL (e.g., Zhang et al. 2022 and reference in).

Mn is sensitive to the prevailing redox conditions in aqueous environments. In addition, recent reports demonstrate that the mid-Proterozoic experienced multiple episodes of sedimentary Mn deposition, an interval that has traditionally been considered to reflect a global "Mn hiatus". Here, we provide direct petrographic and XPS speciation evidence for an active oxidative mechanism during Mn cycling coincident to the deposition of the Wafangzi Mn deposit. Our observations suggest that surface ocean may have had sufficient oxygen concentrations (>10 μM) to support the formation of Mn(IV)-oxides (as well as Fe(III)-(oxyhydr)oxides) along the margin of the Yanliao Basin.

The relative fluxes of organic matter during deposition of Wafangzi Mn deposit provide additional context for the potential for oxygen production during this period. As oxygenic photosynthesis fixes CO_2 as organic carbon, it releases oxygen into the atmosphere and ocean (e.g., Canfield 2014). The buried organic matter then serves as the primary electron donor in DMR and DIR below the sediment–water interface in the

Wafangzi Mn deposit. The content of organic matter preserved now (~1% in the NW ore belt) represents the remainder following a high rate of consumption via DMR and DIR. Thus, the coupled Mn-Fe-C cycles during deposition of the Wafangzi Mn deposit would indicate rather high levels of primary productivity, which may have resulted in the release of appreciable oxygen into the water column and overlying atmosphere.

Combined with other lines of evidence for transient oxygenation from the strata near the center of Yanliao Basin (Hardisty et al. 2017; Tang et al. 2017; Wei et al. 2021; Yu et al. 2022), the wide distribution of Mn-rich strata in the lower Member of the Tieling Formation signify at least a basin-scale increase of oxygen at ~1450 Ma. Moreover, given the widespread nature of contemporaneous Mn deposits, including the 1450 Ma Ullawarra Formation in Western Australia (Spinks et al. 2023), and similar mineralogies to those observed here in the 1.58 Ga Mn deposit, Gaoyuzhuang Formation in North China (Fang et al. 2020) and 1.11 Ga Mn deposit, Ilgarari Formation in Western Australia (Spinks et al. 2023), it is possible that there was possible a transient and widespread swing to higher oxygen levels in the atmosphere and oceans during this interval of the mid-Proterozoic.

Acknowledgments

Funding for this research was provided by the National Natural Science Foundation of China (42172080 and 42202071). Thanks are given to Peng Yuan, Xuerui Fu and Nianqiang Wang for their assistance in fieldwork. The authors would like to acknowledge Sam Spinks and an anonymous reviewer whose comments greatly

improved the manuscript.

References

Anbar, A.D., and Holland, H.D. (1992) The photochemistry of manganese and the origin of banded iron formations. Geochimica et Cosmochimica Acta, 56, 2595–2603.

Bargar, J.R., Tebo, B.M., and Villinski, J.E. (2000) In situ characterization of Mn(II) oxidation by spores of the marine Bacillus sp strain SG-1. Geochimica et Cosmochimica Acta, 64, 2775–2778.

Bargar, J.R., Tebo, B.M., Bergmann, U., Webb, S.M., Glatzel, P., Chiu, V.Q., and Villalobos, M. (2005) Biotic and abiotic products of Mn(II) oxidation by spores of the marine Bacillus sp. strain SG-1. American Mineralogist, 90, 143–154.

Bekker, A., Planavsky, N.J., Krapež, B., Rasmussen, B., Hofmann, A., Slack, J.F., Rouxel, O.J., and Konhauser, K.O. (2014) Iron formations: their origins and implications for ancient seawater chemistry. In Treatise of Geochemistry (eds. H. D. Holland and K. K. Turekian). Elsevier, pp. 561–628.

Bellefroid, E.J., Hood, A.V.S., Hoffman, P.F., Thomas, M.D., Reinhard, C.T., and Planavsky, N.J. (2018) Constraints on Paleoproterozoic atmospheric oxygen levels. Proceedings of the National Academy of Sciences, 115, 8104–8109.

Brand, U., and Veizer, J. (1980) Chemical diagenesis of a multicomponent carbonate system; 1, Trace elements. Journal of Sedimentary Research, 50, 1219–1236.

Brasier, M.D., and Lindsay, J.F. (1998) A billion years of environmental stability and the emergence of eukaryotes: new data from northern Australia. Geology 26, 555–558.

Brusnitsyn, A.I. (2006) Mineralogy and metamorphism conditions of manganese ore at the South Faizulino deposit, the southern Urals, Russia. Geology of Ore Deposits, 48, 193–214.

Brusnitsyn, A.I., Starikova, E.V., and Zhukovd, I.G. (2017) Mineralogy of low grade metamorphosed manganese sediments of the Urals: Petrological and geological applications. Ore Geology Reviews, 85, 140–152.

Calvert, S.E., and Pedersen, T.F. (1996) Sedimentary geochemistry of manganese: implications for the environment of formation of manganiferous black shales. Economic Geology, 91, 36–47.

Canfield, D.E. (1998) A new model for Proterozoic ocean chemistry. Nature, 396, 450–453.

Canfield, D.E. (2014) Oxygen: A Four Billion Year History. Princeton: Princeton University Press.

Canfield, D.E., Zhang, S.C., Wang, H.J., Wang, X.M., Zhao, W.Z., Su, J., Bjerrum, C.J., Haxen, E.R., and Hammarlund, E.U. (2018) A Mesoproterozoic iron formation. Proceedings of the National Academy of Sciences, 115, E3895–E3904.

Canfield, D.E., van Zuilen, M.A., Nabhan, S., Bjerrum, C.J., Zhang, S.C., Wang, H.J., and Wang, X.M. (2021) Petrographic carbon in ancient sediments constrains Proterozoic Era atmospheric oxygen levels. Proceedings of the National Academy of Sciences, 118, e2101544118.

Chen, F.G., Pufahl, P.K., Wang, Q.F., Matheson, E.J., Shabaga, B.M., Zhang, Q.Z., Zeng, Y.S., Le, X.W., Ruan, D., and Zhao, Y.T. (2022) A New Model for the Genesis of Carboniferous Mn Ores, Longtou deposit, South China Block. Economic Geology, 117, 107-125.

Chen, G.X., Cheng, Q.M., Lyons, T.W., Shen, J., Agterberg, F., Huang, N., and Zhao, M.L. (2022) Reconstructing Earth's atmospheric oxygenation history using machine learning. Nature Communications, 13, 5862.

Chu, X.L., Zhang, T.G., Zhang, Q.R., and Lyons, T.W. (2007) Sulfur and carbon isotope records from 1700 to 800Ma carbonates of the Jixian section, northern China: Implications for secular isotope variations in Proterozoic seawater and relationships to global supercontinental events. Geochimica et Cosmochimica Acta, 71, 4668–4692.

Cole, D.B., Reinhard, C.T., Wang, X.L., Gueguen, B., Halverson, G.P., Gibson, T., Hodgskiss, M.S., McKenzie, N.R., Lyons, T.W., and Planavsky, N.J. (2016) A shale-hosted Cr isotope record of low atmospheric oxygen during the Proterozoic. Geology, 44, 555–558.

Daye, M.K., Lepac-Ceraj, V., Pajusalu, M., Rowland, S., Farrell-Sherman, A., Beukes, N., Tamura, N., Fournier, G., and Bosak, T. (2019) Light-driven anaerobic microbial oxidation of manganese. Nature, 576, 311–314.

Deirieh, A., Chang, I.Y., Whittaker, M.L., Weigand, S., Keane, D., Rix, J., Germaine, J.T., Joester, D., and Flemings, P.B. (2018) Particle arrangements in clay slurries: The case against the honeycomb structure. Applied Clay Science, 152, 166–172.

Dellwig. O., Leipe, T., März, C., Glockzin, M., Pollehne, F., Schnetger, B., Yakushev, E.V., Böttcher, M.E., and Brumsack, H.J. (2010) A new particulate Mn–Fe–P-shuttle at the redoxcline of anoxic basins. Geochimica et Cosmochimica Acta, 74, 7100–7115.

Diamond, C.W., and Lyons, T.W. (2018) Mid-Proterozoic redox evolution and the possibility of transient oxygenation events. Emerging Topics in Life Sciences, 2, 235–245.

Diamond, C.W., Planavsky, N.J., Wang, C., and Lyons, T.W. (2018) What the ~1.4 Ga Xiamaling Formation can and cannot tell us about the mid-Proterozoic ocean. Geobiology, 16, 219–236.

Dick, G.J., Clement, B.G., Webb, S.M., Fodrie, F.J., Bargar, J.R., and Tebo, B.M. (2009) Enzymatic microbial Mn(II) oxidation and Mn biooxide production in the Guaymas Basin deep-sea hydrothermal plume. Geochimica et Cosmochimica Acta, 73, 6517–6530.

Dong, Z.G., Peng, Z.D., Robbins, L.J., Konhauser, K.O., Zhang, B.L., Zhang, L.C., Li, J., Li, W.J., Zhang, L., and Wang, C.L. (2023) Episodic ventilation of euxinic bottom waters triggers the formation of black shale-hosted Mn carbonate deposits. Geochimica et Cosmochimica Acta, 341, 132-149.

Elzinga, E.J. (2011) Reductive transformation of birnessite by aqueous Mn(II). Environmental Science & Technology, 45, 6366–6372.

Elzinga, E.J., and Kustka, A.B. (2015) A Mn-54 radiotracer study of Mn isotope solid-liquid exchange during reductive transformation of vernadite (d-MnO2) by aqueous Mn (II). Environmental Science & Technology, 49, 4310–4316.

Fan, D.L., Dasgupta, S., Bolten, B.R., Hariya, Y., Momoi, H., Miura, H., Li, J.J., and Roy, S. (1992) Mineralogy and geochemistry of the Proterozoic Wafangzi Ferromanganese deposit, China. Economic Geology, 87, 1430-1440.

Fan, D.L., Ye, J., and Li, J.J. (1999) Geology, mineralogy, and geochemistry of the Middle Proterozoic Wafangzi ferromanganese deposit, Liaoning Province, China. Ore Geology Reviews, 15, 31-53.

Fang, H., Tang, D.J., Shi, X.Y., Lechte, M., Shang, M.H., Zhou, X.Q., and Yu, W.C. (2020) Manganese-rich deposits in the Mesoproterozoic Gaoyuzhuang Formation (ca. 1.58 Ga), North China Platform: Genesis and paleoenvironmental implications. Palaeogeography, Palaeoclimatology, Palaeoecology, 559, 109966.

Flohr, M.J.K., and Huebner, J.S. (1992) Mineralogy and geochemistry of two metamorphosed sedimentary manganese deposits, Sierra-Nevada, California, USA. Lithos, 29, 57–85.

Gao, Z.F., Zhu, X.K., Wang, D., Pan, C.X., Yan, B., and Li, J. (2021) Insights into hydrothermal controls and processes leading to the formation of the Late Ediacaran Gaoyan stratiform manganese-carbonate deposit, Southwest China. Ore Geology Reviews, 139, 104524.

Gilleaudeau, G.J., Frei, R., Kaufman, A.J., Kah, L.C., Azmy, K., Bartley, J.K., Chernyavskiy, P., and Knoll, A.H. (2016) Oxygenation of the mid-Proterozoic atmosphere: clues from chromium isotopes in carbonates. Geochemical Perspectives Letter, 2, 178–187.

Guo, H., Du, Y.S., Kah, L.C., Huang, J.H., Hu, C.Y., Huang, H., and Yu, W.C. (2013) Isotopic composition of organic and inorganic carbon from the Mesoproterozoic Jixian Group, North China: implications for biological and oceanic evolution. Precambrian Research, 224, 169–183.

Halama, M., Swanner, E.D., Konhauser, K.O., and Kappler, A. (2016) Evaluation of siderite and magnetite formation in BIFs by pressure-temperature experiments of Fe(III) minerals and microbial biomass. Earth and Planetary Science Letters, 450, 243-253.

Halevy, I., Alesker, M., Schuster, E.M., Popovitz-Biro, R., and Feldman, Y. (2017) A key role for green rust in the Precambrian oceans and the genesis of iron formations. Nature Geoscience, 10, 135–139.

Hansel, C.M., Zeiner, C.A., Santelli, C.M., and Webb, S.M. (2012) Mn(II) oxidation by an ascomycete fungus is linked to superoxide production during asexual reproduction. Proceedings of the National Academy of Sciences, 109, 12621–12625.

Hardisty, D.S., Lu, Z.L., Bekker, A., Diamond, C.W., Gill, B.C., Jiang, G.Q., Kah, L.C., Knoll, A.H., Loyd, S.J., and Osburn, M.R. (2017) Perspectives on Proterozoic surface ocean redox from iodine contents in ancient and recent carbonate. Earth and Planetary Science Letters, 463, 159–170.

Hausler, K., Dellwig, O., Schnetger, B., Feldens, P., Leipe, T., Moros, M., Pollehne, F., Schonke, M., Wegwerth, A., and Arz, H.W. (2018) Massive Mn carbonate formation in the Landsort Deep (Baltic Sea): hydrographic conditions, temporal succession, and Mn budget calculations. Marine Geology, 395, 260–270.

He, Y.T., Zhu, X.Y., Qiu, Y.F., Li, J., and Zhao, T.P. (2022) Geochemical evidence of shales in the Tieling Formation, North China Craton: Implications for Mesoproterozoic episodic oxygenation events. Acta Petrologica Sinica, 38, 1741-1755 (in Chinese with English abstract).

Herndon, E.M., Havig, J.R., Singer, D.M., McCormick, M.L., and Kump, L.R. (2018) Manganese and iron geochemistry in sediments underlying the redox-stratified Fayetteville Green Lake. Geochimica et Cosmochimica Acta, 231, 50–63.

Holland, H.D. (2002) Volcanic gases, black smokers, and the Great Oxidation Event. Geochimica et Cosmochimica Acta, 66, 3811–3826.

Huang, Q., Pi, D.H., Jiang, S.Y., Liu, D., Yan, H., Mänd, K., Kirsimäe, k., Bishop, B., Robbins, L.J., and Yang, S.S. (2022) The dual role of microbes in the formation of the Malkantu manganese carbonate deposit, NW China: Petrographic, geochemical, and experimental evidence. Chemical Geology, 606, 120992.

Johnson, J.E., Webb, S.M., Thomas, K., Ono, S., Kirschvink, J.L., and Fischer, W.W. (2013) Manganese-oxidizing photosynthesis before the rise of cyanobacteria. Proceedings of the National Academy of Sciences, 110, 11238–11243.

Johnson, J.E., Webb, S.M., Ma, C., and Fischer, W.W. (2016a) Manganese mineralogy and diagenesis in the sedimentary rock record. Geochimica et Cosmochimica Acta, 173, 210–231.

Johnson, J.E., Savalia, P., Davis, R., Kocar, B.D., Webb, S.M., Nealson, K.H., and Fischer, W.W. (2016b) Real-time manganese phase dynamics during biological and abiotic manganese oxide reduction. Environmental Science & Technology, 50, 4248–4258.

Johnson, J.E., Muhling, J.R., Cosmidis, J., Rasmussen, B., and Templeton, A.S. (2018) Low-Fe(III) greenalite was a primary mineral from neoarchean oceans. Geophysical Research Letters, 45, 3182–3192.

Johnson, J.E. (2019) From minerals to metabolisms: Evidence for life before oxygen from the geological record. Advances in Free Radical Biology and Medicine, 140, 126–137.

Jones, C., Nomosatryo, S., Crowe, S.A., Bjerrum, C.J., and Canfield, D.E. (2015) Iron oxides, divalent cations, silica, and the early earth phosphorus crisis. Geology, 43, 135 138.

Kappler, A., Pasquero, C., Konhauser, K.O., and Newman, D.K. (2005) Deposition of banded iron formations by anoxygenic phototrophic Fe(II)-oxidizing bacteria. Geology, 33, 865- 868.

Konhauser, K.O., Hamade, T., Morris, R.C., Ferris, F.G., Southam, G., Raiswell, R., and Canfield, D. (2002) Could bacteria have formed the Precambrian banded iron formations? Geology, 30, 1079-1082.

Konhauser, K.O., Newman, D.K., and Kappler, A. (2005) The potential significance of microbial Fe(III)-reduction during Precambrian banded iron formations. Geobiology, 3, 167-177.

Konhauser, K.O., Planavsky, N.J., Hardisty, D.S., Robbins, L.J., Warchola, T.J., Haugaard, R., Lalonde S.V., Partin, C.A., Oonk, P.B.H., Tsikos, H., Lyons, T.W., Bekker, A., and Johnson, C.M. (2017) Iron formations: a global record of Neoarchaean to Palaeo-proterozoic environmental history. Earth-Science Reviews, 172, 140–177.

Large, R.R., Mukherjee, I., Gregory, D., Steadman, J., Corkrey, R., and Danyushevsky, L.V. (2019) Atmosphere oxygen cycling through the Proterozoic and Phanerozoic. Mineralium Deposita, 54, 485–506.

Learman, D.R., Voelker, B.M., Vazquez-Rodrigues, A.I., and Hansel, C.M. (2011) Formation of manganese oxides by bacterially generated superoxide. Nature Geoscience, 4, 95–98.

Lefkowitz, J.P., Rouff, A.A., and Elzinga, E.J. (2013) Influence of pH on the reductive transformation of birnessite by aqueous Mn(II). Environmental Science & Technology, 47, 10364–10371.

Li, C., Peng, P.A., Sheng, G., Fu, J., and Yan, Y. (2003) A molecular and isotopic geochemical study of Meso-to Neoproterozoic (1.73–0.85 Ga) sediments from the Jixian section, Yanshan Basin, North China. Precambrian Research, 125, 337–356.

Li, Y.L., Konhauser, K.O., Kappler, A., and Hao, X.L. (2013) Experimental low-grade alteration of biogenic magnetite indicates microbial involvement in generation of banded iron formations. Earth and Planetary Science Letters, 361, 229-237.

Li, Y.L., Konhauser, K.O., and Zhai, M.G. (2017) The formation of primary magnetite in the early Archean oceans. Earth and Planetary Science Letters, 466, 103-114.

Lide, D.R. (2004) CRC Handbook of Chemistry and physics. CRC Press.

Lin, H., Szeinbaum, N.H., Dichristina, T.J., and Taillefert, M. (2012) Microbial Mn(IV) reduction requires an initial one-electron reductive solubilization step. Geochimica et Cosmochimica Acta, 99, 179–192.

Lin, Y.T., Tang, D.J., Shi, X.Y., Zhou, X.Q., and Huang, K.J. (2019) Shallow-marine ironstones formed by microaerophilic iron-oxidizing bacteria in terminal Paleoproterozoic. Gondwana Research, 76, 1–18.

Lingappaa, U.F., Monteverdea, D.R., Magyara, J.S., Valentinea, J.S., and Fischera, W.W. (2019) How manganese empowered life with dioxygen (and vice versa). Free Radical Biology and Medicine, 140, 113–125.

Liu, A.Q., Tang, D.J., Shi, X.Y., Zhou, X.Q., Zhou, L.M., Shang, M.H., Li, Y., and Fang, H. (2020a) Mesoproterozoic oxygenated deep seawater recorded by early diagenetic carbonate concretions from the Member IV of the Xiamaling Formation, North China. Precambrian Research, 341, 105667.

Liu, W.N., Hao, J.H., Elzinga, E.J., Piotrowiak, P., Nanda, V., Yee, N., and Falkowski, P.G. (2020b) Anoxic photogeochemical oxidation of manganese carbonate yields manganese oxide. Proceedings of the National Academy of Sciences, 117, 22698–22704.

Lyons, T.W., Diamond, C.W., and Konhauser, K.O. (2020) Shedding light on manganese cycling in the early oceans. Proceedings of the National Academy of Sciences, 117, 25960–25962.

Lu, S.N., Yang, C.L., Li, H.K., and Li, H.M. (2002) A group of rifting events in the terminal Paleoproterozoic in the North China Craton. Gondwana Research, 5, 123–131.

Luo, G.M., Junium, C.K., Kump, L.R., Huang, J.H., Li, C., Feng, Q.L., Shi, X.Y., Bai, X., and Xie, S.C. (2014) Shallow stratification prevailed for ~1700 to ~1300 Ma ocean: evidence from organic carbon isotopes in the North China Craton. Earth and Planetary Science Letters, 400, 219–232.

Luther, G.W. (2010) The role of one- and two-electron transfer reactions in forming thermodynamically unstable intermediates as barriers in multi-electron redox reactions. Aquatic Geochemistry, 16, 395–420.

Lyons, T.W., Reinhard, C.T., and Planavsky, N.J. (2014) The rise of oxygen in Earth's early ocean and atmosphere. Nature, 506, 307–315.

Lyu, D., Deng, Y., Wang, H.J., Zhang, F.L., Ren, R., Gao, Z.Y., Zhou, C.M., Luo, Z., Wang, X.M., Bi, L.N., Zhang, S.C., and Canfield, D.E. (2021) Using cyclostratigraphic evidence to define the unconformity caused by the Mesoproterozoic Qinyu Uplift in the North China Craton. Journal of Asian Earth Sciences, 206, 104608

Madison, A.S., Tebo, B.M., Mucci, A., Sundby, B., and Luther, G.W. (2013) Abundant Mn(III) in porewaters is a major component of the sedimentary redox system. Science, 341, 875–878.

Manceau, A., and Gallup, L.D. (2005) Nanometer-sized divalent manganese-hydrous silicate domains in geothermal brine precipitates. American Mineralogist, 90, 371–381.

Matheson, E.J., and Pufahl, P.K. (2021) Clinton ironstone revisited and implications for Silurian Earth system evolution. Earth-Science Reviews, 215, 103527.

Maynard, J.B. (2010) The chemistry of manganese ores through time: a signal of increasing diversity of earth-surface environments. Economic Geology, 105, 535–552.

Mei, M.X., Yang, F.J., Gao, J.H., and Meng, Q.F. (2008) Glauconites formed in the high-energy shallow-marine environment of the Late Mesoproterozoic: case study from Tieling Formation at Jixian Section in Tianjin, North China. Earth Science Frontiers, 15, 146–158.

Meng, Q.R., Wei, H.H., Qu, Y.Q., and Ma, S.X. (2011) Stratigraphic and sedimentary records of the rift to drift evolution of the northern North China craton at the Paleo- to Mesoproterozoic transition. Gondwana Research, 20, 205–218.

Morgan, J.J. (2005) Kinetics of reaction between O2 and Mn(II) species in aqueous solutions. Geochimica et Cosmochimica Acta, 69, 35–48.

Mucci, A. (2004) The behavior of mixed Ca–Mn carbonates in water and seawater: controls of manganese concentrations in marine porewaters. Aquatic Geochemistry, 10, 139–169.

Neumann, T., Heiser, U., Leosson, M.A., and Kersten, M. (2002) Early diagenetic processes during Mn-carbonate formation: evidence from the isotopic composition of authigenic Carhodochrosites of the Baltic Sea. Geochimica et Cosmochimica Acta, 66, 867–879.

Nims, C., and Johnson, J.E. (2022) Exploring the secondary mineral products generated by microbial iron respiration in Archean ocean simulations. Geobiology, 20, 743–763.

Nishida, N., Ito, M., Inoue, A., and Takizawa, S. (2013) Clay fabric of fluid-mud deposits from laboratory and field observations: Potential application to the stratigraphic record. Marine Geology, 337, 1–8.

Oldham, V.E., Mucci, A., Tebo, B.M., and Luther, G.W. (2017) Soluble Mn(III)-L complexes are abundant in oxygenated waters and stabilized by humic ligands. Geochimica et Cosmochimica Acta, 199, 238–246.

Olson, J.M. (1970) The Evolution of Photosynthesis. Science, 168, 438–446.

Ossa, F.O., Hofmann, A., Wille, M., Spangenberg, J.E., Bekker, A., Poulton, S.W., Eickmann, B., and Schoenberg, R. (2018) Aerobic iron and manganese cycling in a redox stratified Mesoarchean epicontinental sea. Earth and Planetary Science Letters, 500, 28–40.

Ostrander, C.M., Nielsen, S.G., Owens, J.D., Kendall, B., Gordon, G.W., Romaniello, S.J., and Anbar, A.D. (2019) Fully oxygenated water columns over continental shelves before the Great Oxidation Event. Nature Geoscience, 12, 186–191.

Parker, D.L., Takami, M., Mylene, L., Mozafarzadeh, R.V., McCarthy, J.K., and Tebo, B.M. (2007) Inter-relationships of MnO_2 precipitation, siderophore–Mn(III) complex formation, siderophore degradation, and iron limitation in Mn(II)-oxidizing bacterial cultures. Geochimica et Cosmochimica Acta, 71, 5672–5683.

Partin, C.A., Bekker, A., Planavsky, N.J., Scott, C.T., Gill, B.C., Li, C., Podkovyrov, V., Maslov, V., Konhauser, K.O., Lalonde, S.V., Love, G.D., Poulton, S.W., and Lyons, T.W. (2013) Large-scale fluctuations in Precambrian atmospheric and oceanic oxygen levels from the record of U in shales. Earth and Planetary Science Letters, 369, 284-293.

Phoenix, V.R., Konhauser, K.O., and Ferris, F.G. (2003) Experimental study of iron and silica immobilization by bacteria in mixed Fe-Si systems: Implications for microbial silicification in hot-springs. Canadian Journal of Earth Sciences, 40, 1669-1678.

Planavsky, N.J., McGoldrick, P., Scott, C.T., Li, C., Reinhard, C.T., Kelly, A.E., Chu, X.L., Bekker, A., Love, G.D., and Lyons, T.W. (2011) Widespread iron-rich conditions in the mid-Proterozoic ocean. Nature, 477, 448–451.

Planavsky, N.J., Asael, D., Hofmann, A., Reinhard, C.T., Lalonde, S.V., Knudsen, A., Wang, X., Ossa, O.F., Pecoits, E., Smith, A.J.B., Beukes, N.J., Bekker, A., Johnson, T.M., Konhauser, K.O., Lyons, T.W., and Rouxel, O.J. (2014a) Evidence for oxygenic photosynthesis half a billion years before the Great Oxidation Event. Nature Geoscience, 7, 283–286.

Planavsky, N.J., Reinhard, C.T., Wang, X.L., Thomson, D., McGoldrick, P., Rainbird, R.H., Johnson, T., Fischer, W.W., and Lyons, T.W. (2014b) Low Mid-Proterozoic atmospheric oxygen levels and the delayed rise of animals. Science, 346, 635–638.

Planavsky, N.J., Cole, D.B., Isson, T.T., Reinhard, C.T., Crockford, P.W., Sheldon, N.D., and Lyons, T.W. (2018) A case for low atmospheric oxygen levels during Earth's middle history. Emerging Topics in Life Sciences, 2, 149–159.

Planavsky, N.J., Crowe, S.A., Fakhraee, M., Beaty, B., Reinhard, C.T., Mills, B.J.W., Holstege, C., and Konhauser, K.O. (2021) The evolution of the size and scope of Earth's biosphere. Nature Reviews Earth and Environment, 2, 123–139.

Poulton, S.W., and Canfield, D.E. (2011) Ferruginous conditions: a dominant feature of the ocean through Earth's history. Elements, 7, 107–112.

Qu, Y.Q., Pan, J.G., Ma, S.X., Lei, Z.P., Li, L., and Wu, G.L. (2014) Geological characteristics and tectonic significance of unconformities in Mesoproterozoic successions in the northern margin of the North China Block. Geoscience Frontiers, 5, 127–138.

Rasmussen, B., Krapež, B., and Meier, D.B. (2014) Replacement origin for hematite in 2.5 Ga banded iron formation: Evidence for post depositional oxidation of iron-bearing minerals. Geological Society of America Bulletin, 126, 438–446.

Rasmussen, B., Muhling, J.R., Suvorova, A., and Krapež, B. (2017) Greenalite precipitation linked to the deposition of banded iron formations downslope from a late Archaean carbonate platform. Precambrian Research, 290, 49–62.

Reinhard, C.T., Planavsky, N.J., Robbins, L.J., Partin, C.A., Gill, B.C., Lalonde, S.V., Bekker, A., Konhauser, K.O., and Lyons, T.W. (2013) Proterozoic ocean redox and biogeochemical stasis. Proceedings of the National Academy of Sciences, 110, 5357–5362.

Robbins, L.J., Fakhraee, M., Smith, A.J.B., Bishop, B.A., Swanner, E.D., Peacock, C., Wang, C.L., Planavksy, N.J., Reinhard, C.T., Crowe, S.A., and Lyons, T.W. (2023) Manganese oxides, Earth surface oxygenation, and the rise of oxygenic photosynthesis. Earth-Science Reviews, 104368.

Roy, S. (2006) Sedimentary manganese metallogenesis in response to the evolution of the Earth system. Earth-Science Reviews, 77, 273–305.

Schad, M., Konhauser, K.O., Sɑ́nchez-Baracaldo, P., Kappler, A., and Bryce, C. (2019) How did the evolution of oxygenic photosynthesis influence the temporal and spatial development of the microbial iron cycle on ancient Earth? Free Radical Biology and Medicine, 140, 154-166.

Schippers, A., Neretin, L.N., Lavik, G., Leipe, T., and Pollehne, F. (2005) Manganese (II) oxidation driven by lateral oxygen intrusions in the western Black Sea. Geochimica et Cosmochimica Acta, 69, 2241–2252.

Shang, M.H., Tang, D.J., Shi, X.Y., Zhou, L.M., Zhou, X.Q., Song, H.Y., and Jiang, G.Q. (2019) A pulse of oxygen increase in the early Mesoproterozoic ocean at ca. 1.57–1.56 Ga. Earth and Planetary Science Letters, 527, 115797.

Siahi, M., Tsikos, H., Rafuza, S., Oonk, P.B., Mhlanga, X.R., van Niekerk, D., Mason, P.R., and Harris, C. (2020) Insights into the processes and controls on the absolute abundance and distribution of manganese in Precambrian iron formations. Precambrian Research, 350, 105878.

Smith, A.J.B., and Beukes, N.J. (2023) The paleoenvironmental implications of pre-Great Oxidation Event manganese deposition in the Mesoarchean Ijzermijn Iron Formation Bed, Mozaan Group, Pongola Supergroup, South Africa. Precambrian Research, 384, 106922.

Spinks, S.C., Sperling, E.A., Thorne, R.L., LaFountain, F., White, A.J.R., Armstrong, J., Woltering, M., and Ian M. Tyler, I.M. (2023) Mesoproterozoic surface oxygenation accompanied major sedimentary manganese deposition at 1.4 and 1.1 Ga. Geobiology, 21, 28–43.

Sun, S., Konhauser, K.O., Kappler, A., and Li, Y.L. (2015) Primary hematite in Neoarchean to Paleoproterozoic oceans. Geological Society of America Bulletin, 127, 850–861.

Su, W.B., Li, H.K., Huff, W.D., Ettensohn, F.R., Zhang, S.H., Zhou, H.Y., and Wan, Y.S. (2010) SHRIMP U-Pb dating for a K-bentonite bed in the Tieling Formation, North China. Chinese Science Bulletin, 55, 3312–3323.

Tang, D.J., Shi, X.Y., Wang, X.Q., and Jiang, G.Q. (2016) Extremely low oxygen concentration in midProterozoic shallow seawaters. Precambrian Research, 276, 145–157.

Tang, D.J., Shi, X.Y., Ma, J.B., Jiang, G.Q., Zhou, X.Q., and Shi, Q. (2017) Formation of shallow-water glaucony in weakly oxygenated Precambrian ocean: An example from the Mesoproterozoic Tieling Formation in North China. Precambrian Research, 294, 214–229.

Tang, D.J., Shi, X.Y., Jiang, G.Q., Wu, T., Ma, J.B., and Zhou, X.Q. (2018) Stratiform siderites from the Mesoproterozoic Xiamaling Formation in North China: Genesis and environmental implications. Gondwana Research, 58, 1–15.

Tang, D.J., Ma, J.B., Shi, X.Y., Lechte, M., and Zhou, X.Q. (2020) The formation of marine red beds and iron cycling on the Mesoproterozoic North China Platform. American Mineralogist, 105, 1412–1423.

Tebo, B.M., Bargar, J.R., Clement, B.G., Dick, G.J., Murray, K.J., Parker, D., Verity, R., and Webb, S.M. (2004) Biogenic manganese oxides: properties and mechanisms of formation. Annual Review of Earth and Planetary Sciences, 32, 287–328.

Tebo, B.M., Johnson, H.A., McCarthy, J.K., and Templeton, A.S. (2005) Geomicrobiology of manganese(II) oxidation. Trends in Microbiology, 13, 421–428.

Tostevin, R., Wood, R., Shields, G., Poulton, S., Guilbaud, R., Bowyer, F., Penny, A., He, T., Curtis, A., and Hoffmann, K. (2016) Low-oxygen waters limited habitable space for early animals. Nature Communications, 7, 12818.

Trouwborst, R.E., Clement, B.G., Tebo, B.M., Glazer, B.T., and Luther, G.W. (2006) Soluble Mn(III) in suboxic zones. Science, 313, 1955–1957.

Tsikos, H., Beukes, N.J., Moore, J.M., and Harris, C. (2003) Deposition, Diagenesis, and Secondary Enrichment of Metals in the Paleoproterozoic Hotazel Iron Formation, Kalahari Manganese Field, South Africa. Economic Geology and the Bulletin of the Society of Economic Geologists, 98, 1449–1462.

Van Cappellen, P., and Wang, Y.F. (1996) Cycling of iron and manganese in surface sediments; a general theory for the coupled transport and reaction of carbon, oxygen, nitrogen, sulfur, iron, and manganese. American Journal of Science, 296, 197–243.

Van Cappellen, P., Viollier, E., Roychoudhury, A., Clark, L., Ingall, E., Lowe, K., and Dichristina, T. (1998) Biogeochemical cycles of manganese and iron at the oxic−anoxic transition of a stratified Marine Basin (Orca Basin, Gulf of Mexico). Environmental Science & Technology, 32, 2931–2939.

Wang, H.Y., Zhang, Z.H., Li, C., Algeo, T.J., Cheng, M., and Wang, W. (2020)

Spatiotemporal redox heterogeneity and transient marine shelf oxygenation in the Mesoproterozoic ocean. Geochimica et Cosmochimica Acta, 270, 201–217.

Webb, S.M., Dick, G.J., Bargar, J.R., and Tebo, B.M. (2005) Evidence for the presence of Mn(III) intermediates in the bacterial oxidation of Mn(II). Proceedings of the National Academy of Sciences, 102, 5558–5563.

Wei, W., Frei, R., Klaebe, R., Tang, D.J., Wei, G.Y, Li, D., Tian, L.L., Huang, F., and Ling, H.F. (2021) A transient swing to higher oxygen levels in the atmosphere and oceans at ~1.4 Ga. Precambrian Research, 354, 106058.

Wittkop, C., Swanner, E.D., Grengs, A., Lambrecht, N., Fakhraee, M., Myrbo, A., Bray, A.W., Poulton, S.W., and Katsev, S. (2020) Evaluating a primary carbonate pathway for manganese enrichments in reducing environments. Earth and Planetary Science Letters, 538 116201.

Yan, H., Pi, D.H., Jiang, S.Y., Mao, J.W., Xu, L.G., Yang, X.Q., Hao, W.D., Mand, K., Li, L., Konhauser, K.O., and Robbins, L.J. (2022) Mineral paragenesis in Paleozoic manganese ore deposits: Depositional versus post-depositional formation processes. Geochimica et Cosmochimica Acta, 325, 65-86.

Yu, Y., Chen, Y.L., Li, D.P., and Su, J.T. (2022) A transient oxygen increase in the Mesoproterozoic ocean at ~1.44 Ga: Geochemical evidence from the Tieling Formation, North China Platform. Precambrian Research, 369, 106527.

Zhai, M.G., Zhu, X.Y., Zhou, Y.Y., Zhao, L., and Zhou, L.G. (2020) Continental crustal evolution and synchronous metallogeny through time in the North China Craton. Journal of Asian Earth Sciences, 194, 104169.

Zhang, B.L., Wang, C.L., Robbins, L.J., Zhang, L.C., Konhauser, K.O., Dong, Z.G., Li, W.J., Peng, Z.D., and Zheng, M.T. (2020) Petrography and geochemistry of the Carboniferous Ortokarnash Manganese deposit in the Western Kunlun Mountains, Xinjiang Province, China: Implications for the depositional environment and the origin of mineralization. Economic Geology, 115, 1559-1588.

Zhang, K., Zhu, X.K., Wood, R.A., Shi, Y., Gao, Z.F., and Poulton, S.W. (2018) Oxygenation of the Mesoproterozoic ocean and the evolution of complex eukaryotes. Nature Geoscience, 11, 345–350.

Zhang, S.C., Wang, X.M., Hammarlund, E.U., Wang, H.J., Costa, M.M., Bjerrum, C.J., Connelly, J.N., Zhang, B.M., Bian, L.Z., and Canfield, D.E. (2015) Orbital forcing of climate 1.4 billion years ago. Proceedings of the National Academy of Sciences, 112, E1406–E1413.

Zhang, S.C., Wang, X.M., Wang, H.J., Bjerrum, C.J., Hammarlund, E.U., Costa, M.M., Connelly, J.N., Zhang, B.M., Su, J., and Canfield, D.E. (2016) Sufficient oxygen for animal respiration 1,400 million years ago. Proceedings of the National Academy of Sciences, 113, 1731–1736.

Zhang, S.C., Wang, X.M., Wang, H.J., Hammarlund, E.U., Su, J., Wang, Y., and Canfield, D.E. (2017) The oxic degradation of sedimentary organic matter 1400 Ma constrains atmospheric oxygen levels. Biogeosciences, 14, 2133–2149.

Zhang, S.C., Wang, X.M., Wang, H.J., Bjerrum, C.J., Hammarlund, E.U., Haxen, E.R., Wen, H.J., Ye, Y.T., and Canfield, D.E. (2019) Paleoenvironmental proxies and what the Xiamaling Formation tells us about the mid-Proterozoic ocean.

Geobiology, 17, 225–246.

Zhang, S.C., Wang, H.J., Wang, X.M., and Ye, Y.T. (2021) The Mesoproterozoic Oxygenation Event. Science China Earth Sciences, 64, 2043–2068.

Zhao, G.C., and Zhai, M.G. (2013) Lithotectonic elements of Precambrian basement in the North China Craton: review and tectonic implications. Gondwana Research, 23, 1207–1240.

Zuo, P.F., Li, Y., Zhang, G.H., Si, R.J., Wang, S.Y., Liu, S.C., Zheng, D.H., and Sun, J.T. (2019) Reviews of the Mesoproterozoic to Neoproterozoic sedimentary sequences and new constraints on the tectono-sedimentary evolution of the southern margin of the North China Craton. Journal of Asian Earth Sciences, 179, 416–429.

Table 1: The quantitative curve fit results for XPS by Mn 2p, Mn 3s and Fe 2p spectra of southeast (SE) and northwest (NW) samples from Wafangzi manganese deposit.

Sample			Mn3s	Mn2p			Fe2p	
			ΔBinding Energy (E)	fraction (%)			fraction (%)	
				Mn(II)	Mn(III)	Mn(IV)	Fe(II)	Fe(III)
Southeast	lower ore bed	SE-2	6.0	100	-	-	-	100
		SE-3	5.9	100	-	-	-	100
		SE-5	5.7	73.57	26.43	-		
		SE-6	5.7	76.60	23.40	-		
		SE-7	5.9	100	-	-		
	interlayer	SE-8					-	100
	middle ore bed	SE-9	5.5	-	100	-		
		SE-10	5.5	-	95.33	4.67		
		SE-11	5.4	-	84.53	15.47	-	100
		SE-12	5.5	-	100	-	-	100
	upper ore bed	SE-13	5.7	67.93	32.07	-		
		SE-14	5.7	68.77	31.23	-		
Northwest	lower ore bed	NW-2	6.0	100	-	-	100	-
	middle ore bed	NW-5	5.9	100	-	-	48.14	51.86
		NW-6					52.32	47.68

“Blank”: untested data; “-”: representation 0.

Table 2: Manganese and iron concentrations, Mn/Fe and Fe/Al ratios, carbon isotope composition, and total organic carbon contents of bulk southeast (SE) and northwest (NW) samples from Wafangzi manganese deposit.

Samples	Mn (wt%)	Fe (wt%)	Mn/Fe (wt%,ratios)	Fe/Al (wt%,ratios)	$\delta^{13}C_{carb}$ (‰,VPDB)	TOC (%)
SE-2	20.87	6.32	3.30	5.02	-4.3	0.22
SE-3	25.77	6.89	3.74	6.13	-4.0	0.15
SE-5	30.42	1.69	18.00	1.58	-4.6	0.12
SE-6	28.86	1.58	18.27	1.81	-3.9	0.15
SE-7	27.89	4.76	5.86	3.04	-4.2	0.15
SE-8	10.48	7.66	1.37	2.78	-4.6	0.17
SE-9	38.23	2.56	14.93	3.60	-	0.10
SE-10	23.58	2.32	10.16	1.09	-	0.09
SE-11	35.89	6.34	5.66	3.29	-	0.07
SE-13	32.56	2.34	13.91	2.03	-	0.06
NW-2	25.48	11.57	2.20	10.03	-7.2	0.81
NW-3	23.51	12.76	1.84	14.21	-6.5	0.86
NW-4	24.38	10.01	2.44	8.97	-6.3	0.97
NW-5	21.66	15.51	1.40	14.12	-5.2	0.91
NW-6	20.96	15.25	1.37	12.40	-6.8	0.77

“Blank”: Untested sample.

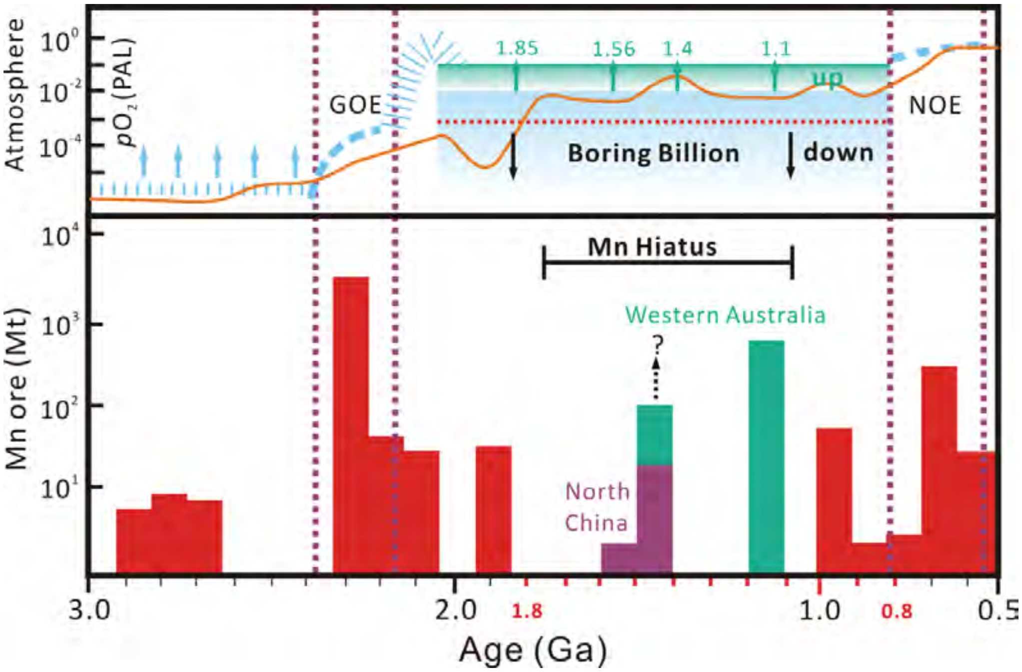

Fig.1: Distribution of Precambrian sedimentary manganese ores, compiled by mass, in the context of atmospheric oxygenation (modified from Bekker et al. 2014). GOE—Great Oxidation Event; NOE—Neoproterozoic Oxidation Event; purple dashed lines bracket oxidation events. Historically, a pronounced Mn hiatus has been proposed to correspond to the mid-Proterozoic (ca. 1.8-0.8 Ga) a period also characterized by low levels of atmospheric oxygen levels (e.g., Planavsky et al. 2011, 2014b, 2018; Reinhard et al. 2013; Lyons et al. 2014; Cole et al. 2016; blue region in top panel). However, an increasing number of studies (e.g., Zhang et al. 2022 and reference in) from globally distributed marine basins and an machine learning model based on mafic igneous deposits (Chen et al. 2022; orange full line in top panel) suggest that there were several pulsed episodes of oxygenation events during this interval (green region in top panel). The mid-Proterozoic also saw multiple episodes of sedimentary Mn deposition (~ 1.5 Ga and ~ 1.1Ga) from North China (purple square; Fan et al. 1992, 1999; Fang et al. 2020) and Western Australia (green square; Spinks et al. 2022), respectively. An accurate tonnage resource estimate for 1.45 Ga Mn deposition from Western Australia is lacking. But for now, the tonnages of sedimentary Mn during mid-Proterozoic exceed that of any period of the Neoproterozoic and most of the Paleoproterozoic.

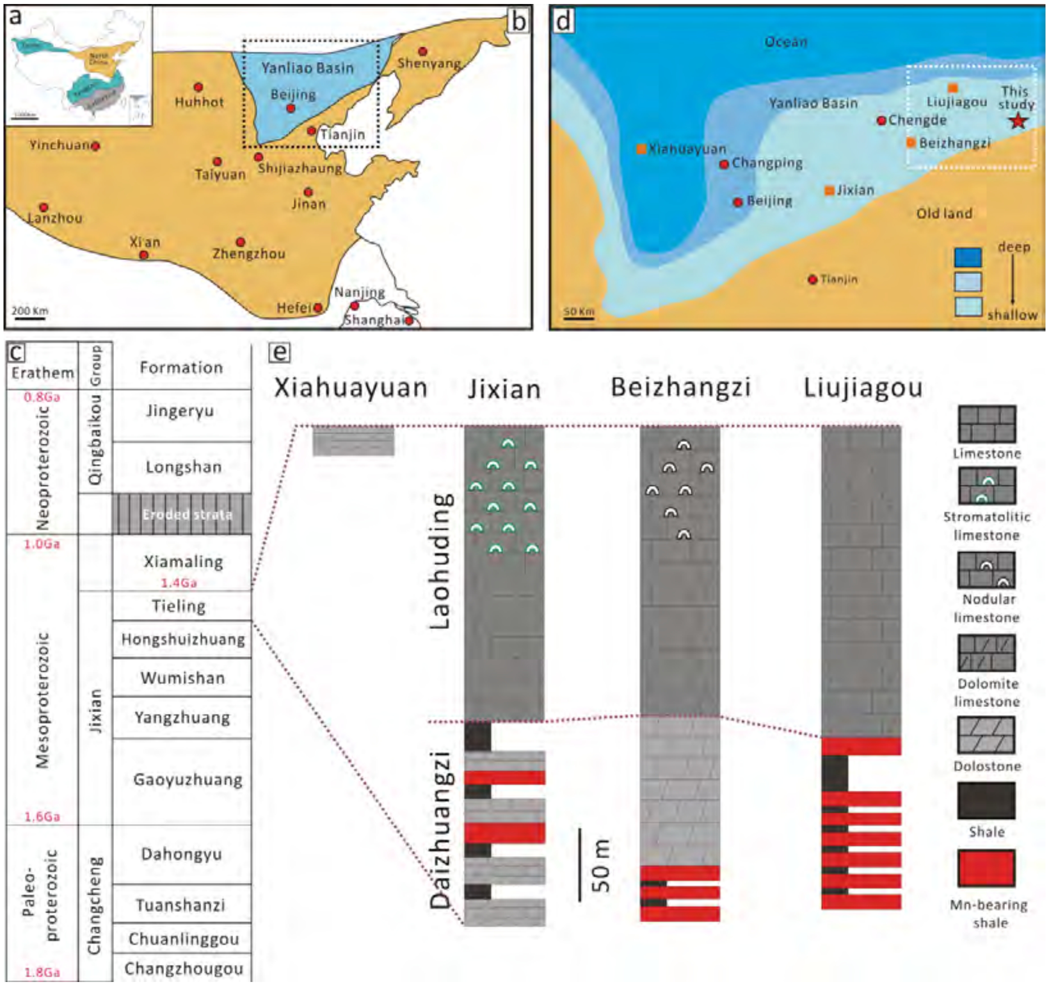

Fig. 2: (a) Present position and range of the North China Craton. (b) The range of the Yanliao Basin in the North China Craton, modified from Lyu et al. (2021). (c) Stratigraphic column of mid-Proterozoic Yanliao Basin in the North China Craton. Ages are from Lyu et al. (2021). (d) Paleogeography of the Yanliao Basin during the Mesoproterozoic Tieling and Xiamaling Formations (1.45–1.35 Ga), highlighting several of the representative sections (orange squares) from deep to shallow water depositional environments. Red circles indicate local cities. White box identifies the study region. (e) Stratigraphy of representative sections from (d) corresponding to the Tieling Formation, modified from Lyu et al. (2021). Noteworthy, is that manganese-rich strata are generally developed in the lower member of the Tieling Formation and tend to thicken and mineralize along the northeastern margin of the Yanliao Basin where there is more shale and less interlayered dolostone.

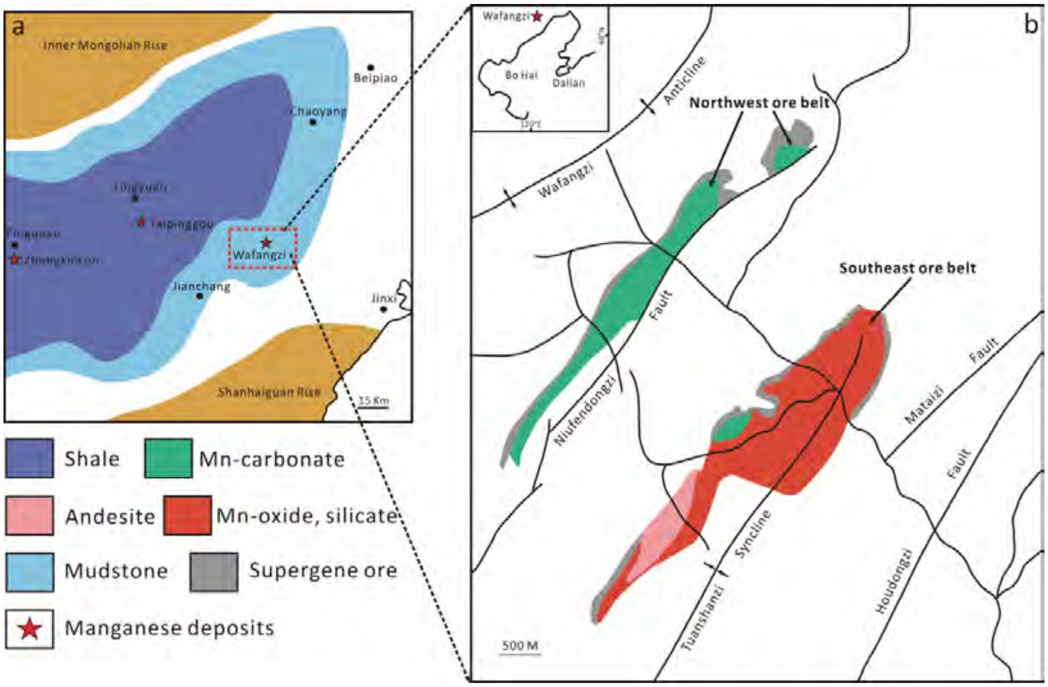

Fig. 3: (a) Lithofacies distribution, paleogeography, and Mn deposits (red stars) from the study region associated with the Tieling Formation on the northeastern margin of the Yanliao Basin, modified from Fan et al. (1999). Red rectangle indicates the location of the studied region. (b) The lithological and mineralogical distribution within the northwest and southeast ore belts of the Wafangzi Mn district. In lower left corner legend, Mn-oxide represent the primary minerals, while supergene ore (pyrolusite; MnO_2) is regard as secondary weathering product.

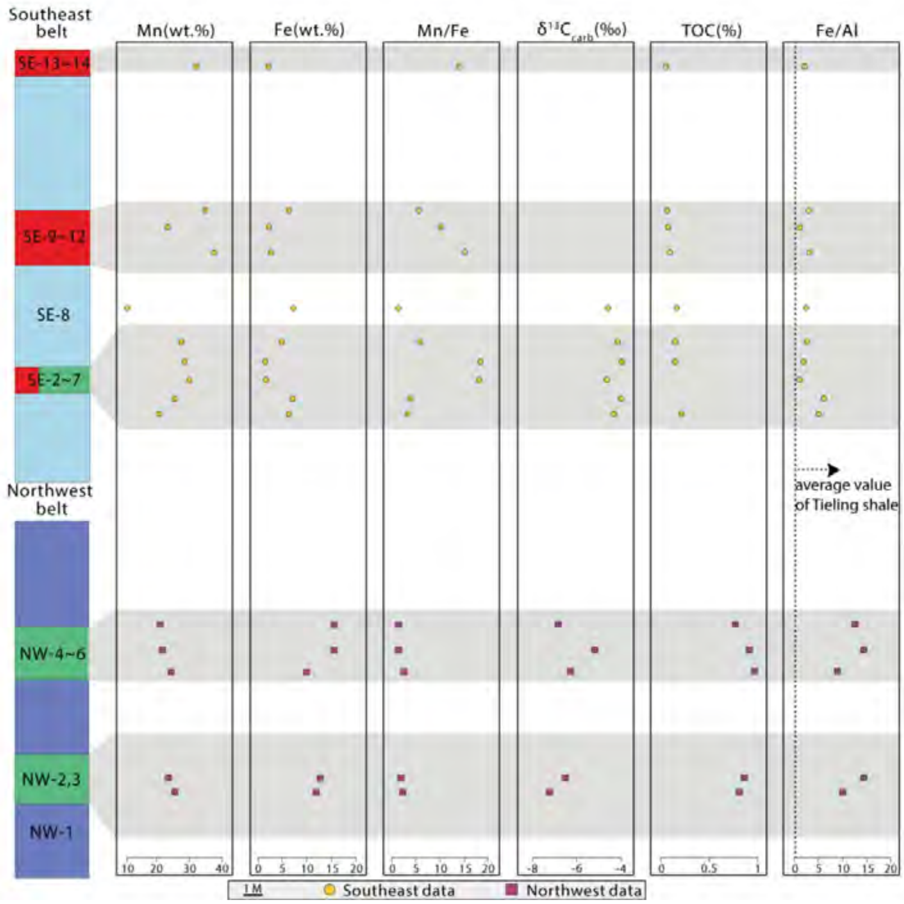

Fig. 4: Simplified stratigraphy and correlation of the northwest and southeast Wafangzi ore belts along with relative sampling locations, highlighting the chemostratigraphic distribution of Mn, Fe, Mn/Fe and Fe/Al ratios, carbon isotopic compositions ($\delta^{13}C$), and total organic carbon (TOC). Vertical lines on Fe/Al plots are based on the data from He et al. (2022). Refer to Fig 3 for the legend.

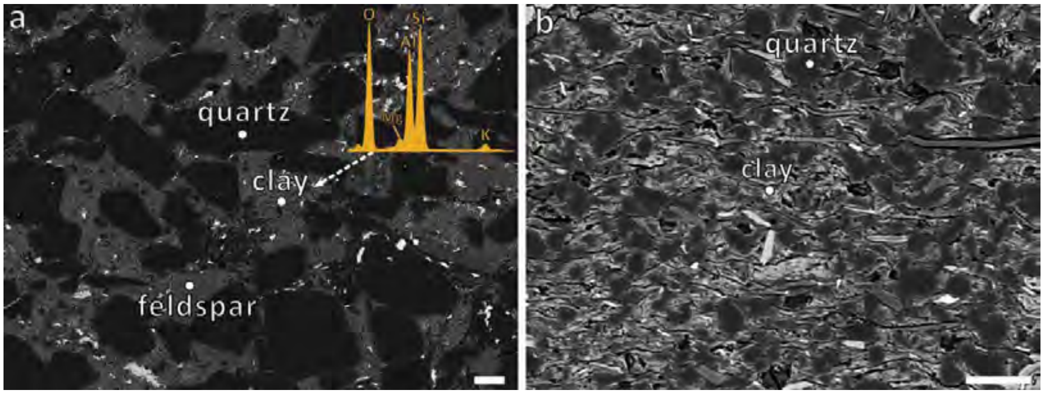

Fig. 5: Back-scattered electron (BSE)-SEM images of wall rock samples southeast (SE)-1 (a) and northwest (NW)-2 (b) indicating samples are mainly composed of detrital quartz with different degrees of rounding, size, and variable clay minerals. Only sample SE-1 contains detrital feldspar. Scale bars represent 20 μm.

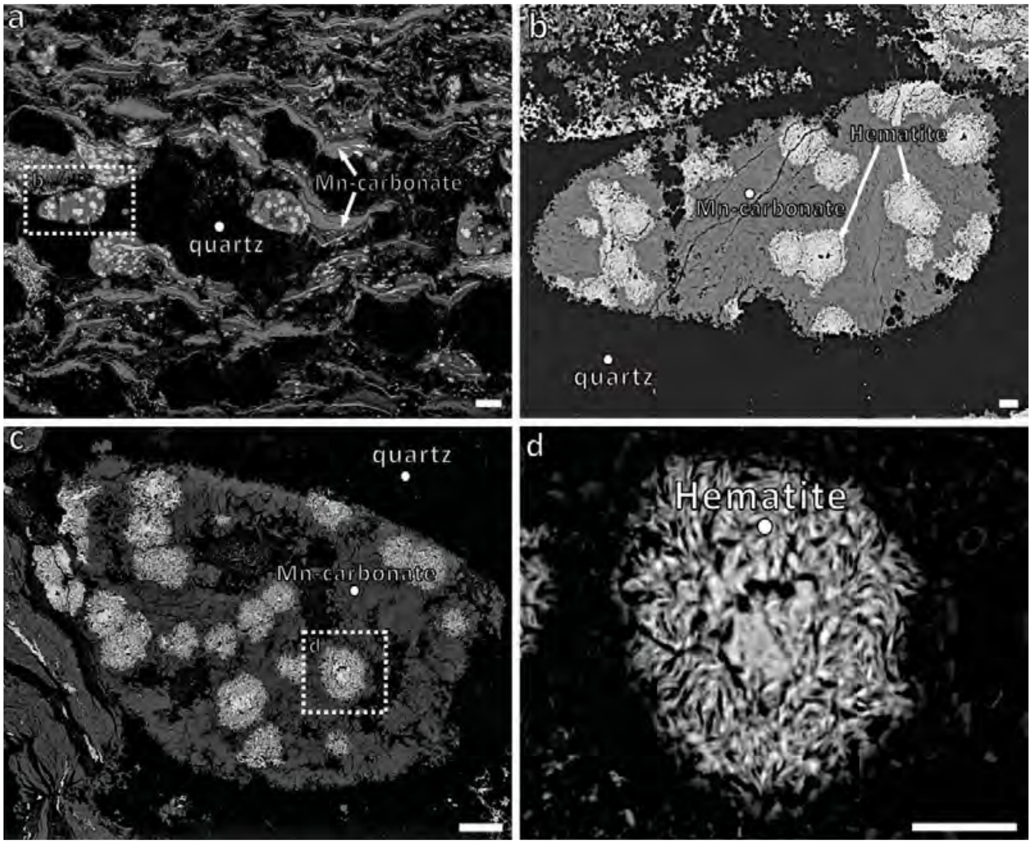

Fig. 6: (a) Back-scattered electron (BSE)-SEM images of sample southeast (SE)-2 from the lower ore bed displaying Mn-carbonate cement that solidifies quartz grains and is concentrated in residual pore space. (b) Magnified image of the area indicated in panel a, showing spheroidal hematite clusters in Mn(II)-carbonate nodules. Similar features present in (c) are highlighted in (d). Scale bars represent 10 μm.

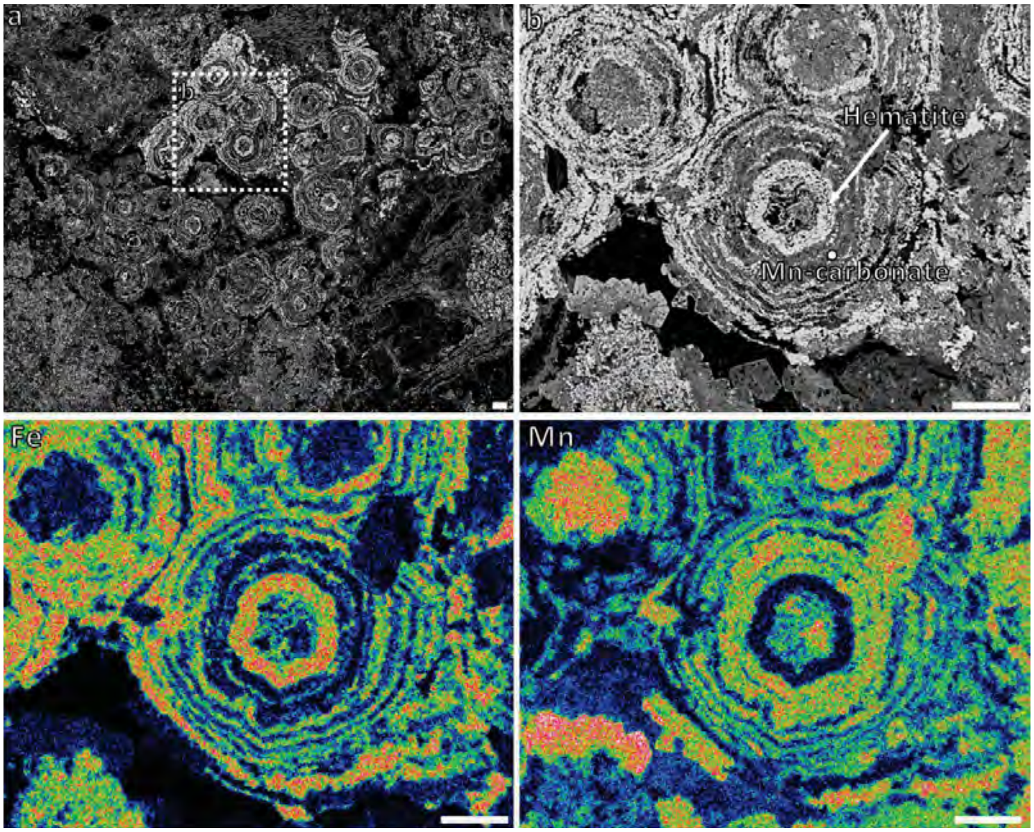

Fig. 7: (a-b) Back-scattered electron (BSE)-SEM images of sample southeast (SE)-3 from the lower ore bed showing grains with concentric rings of hematite and Mn-carbonate. Bottom figs: Energy dispersive spectrum (EDS) maps of panel b showing relative Fe and Mn content, respectively. Scale bars are10 μm.

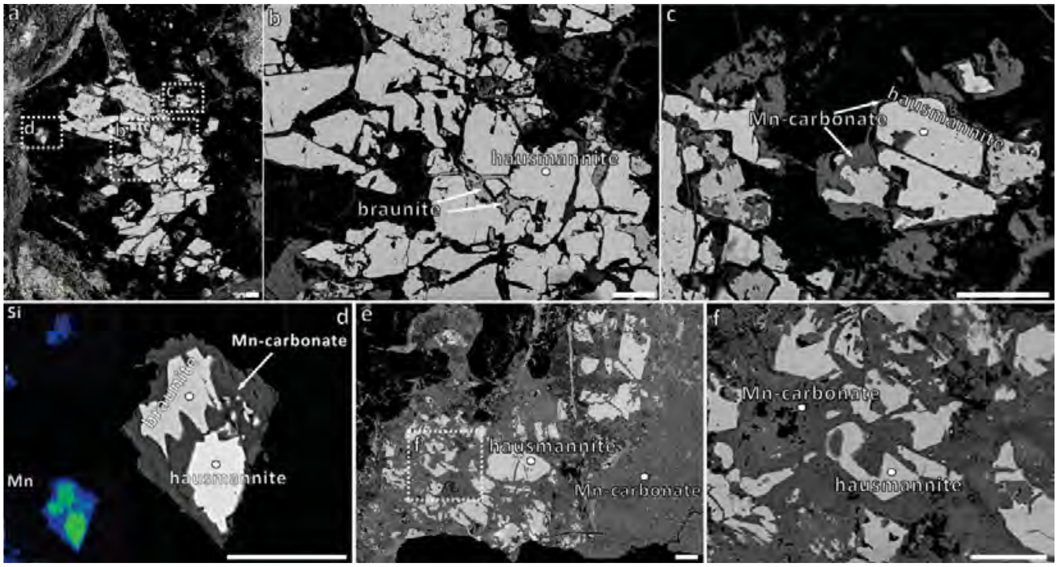

Fig. 8: (a) Back-scattered electron (BSE)-SEM images of sample southeast (SE)-4 from the lower ore bed showing the contact relationship between Mn-oxide, silicate (white), and carbonate (grey) minerals phases. (b) Magnified image of the area indicated in panel (a), showing braunite that clearly cross-cuts hausmannite. (c) Magnified image of the area indicated in panel (a) showing Mn-carbonate eroding hausmannite along the rim of the hausmannite grains. (d) Magnified image of the area indicated in panel (a), showing the presence of hausmannite and braunite as inclusions, or unreacted residues, within Mn-carbonate. The top left and bottom left corner in d show energy dispersive spectrum (EDS) maps of relative Si and Mn content, respectively. (e-f) Unreacted residues of hausmannite replaced by Mn-carbonate. Scale bars represent 10 µm.

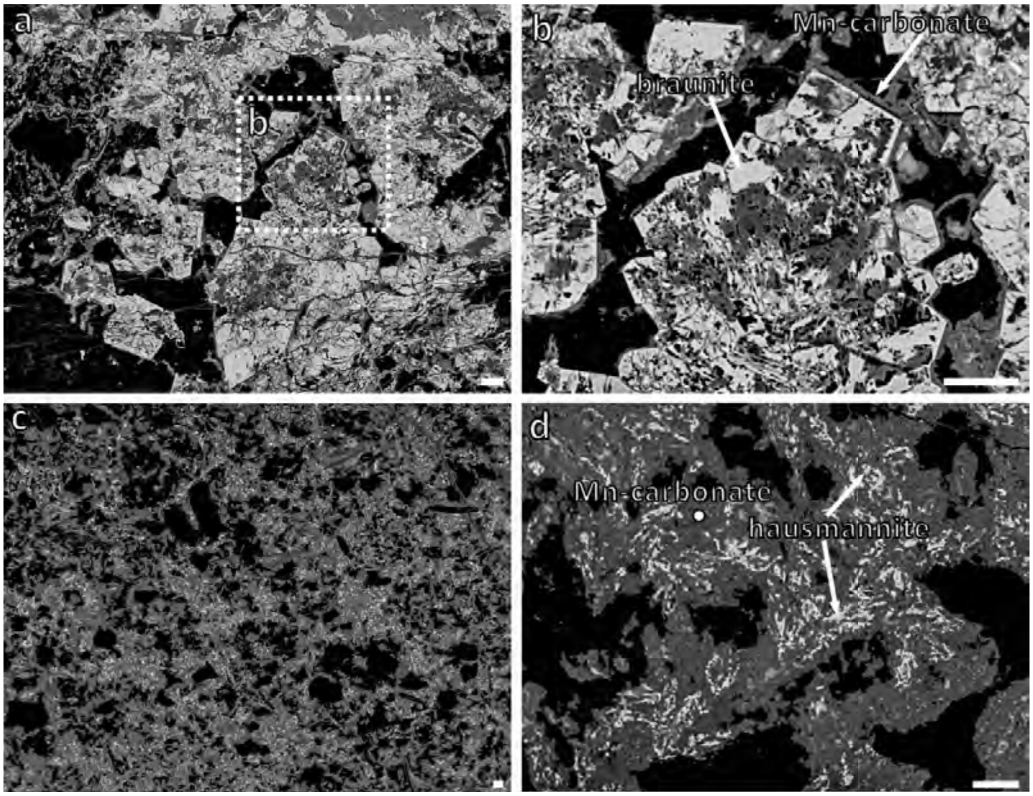

Fig. 9: Back-scattered electron (BSE)-SEM images of sample southeast (SE)-5 and 6 from the lower ore bed. (a) SE-5 showing the contact relationship between braunite and Mn-carbonate minerals phases. (b) Magnified image of the area indicated in panel (a) where Mn-carbonate has destroyed the subhedral habit of braunite. Alteration appears to have occurred along the rim of the braunite grains. (c-d) SE-6 showing hausmannite as disseminated inclusions within a Mn-carbonate assemblage. Scale bars represent 10 µm.

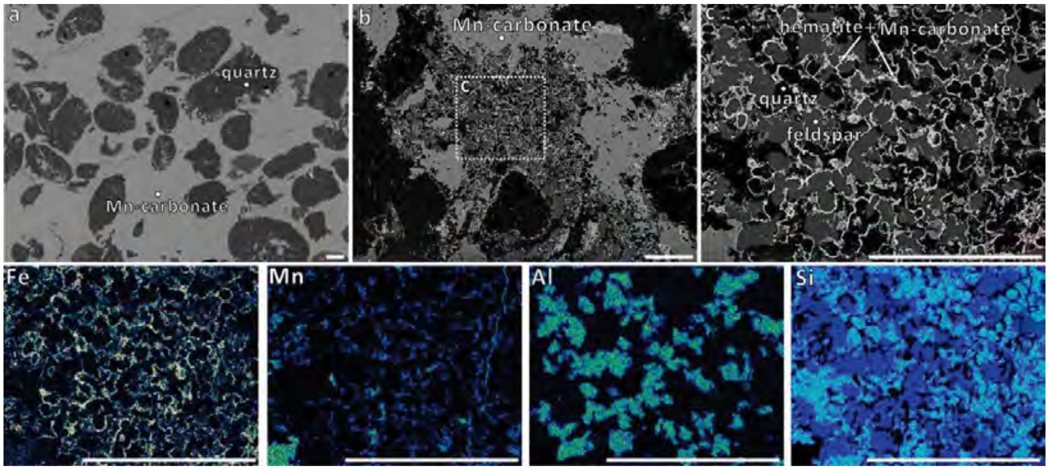

Fig. 10: (a-b) Back-scattered electron (BSE)-SEM images of sample southeast (SE)-7 from the lower ore bed showing Mn-carbonate as a cement solidified quartz grains. (c) Magnified image of the area indicated in panel (b) showing hematite with Mn-carbonate along the rim of detrital quartz and feldspar. Bottom figs: Energy dispersive spectrum (EDS) maps of relative Fe, Mn, Al, and Si content (left to right, respectively) from the region in panel (c). Scale bars represent 100 μm.

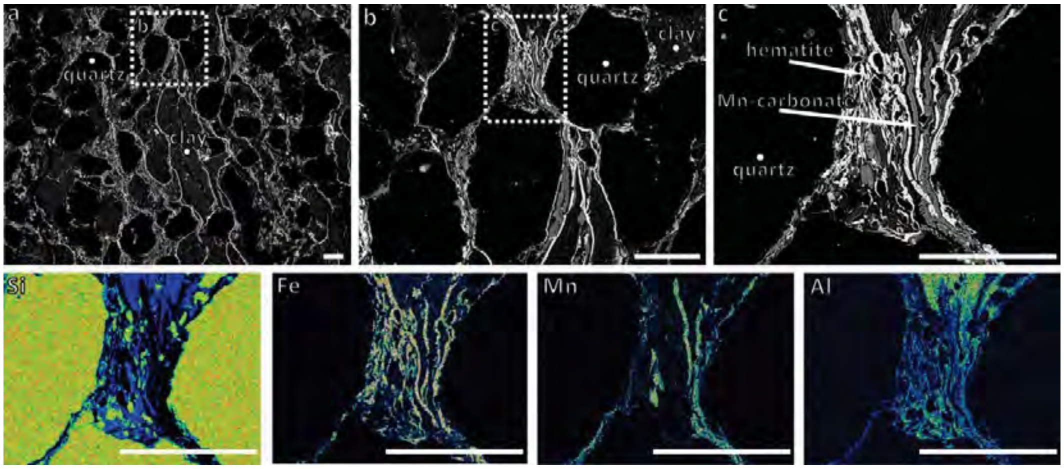

Fig. 11: (a-c) Back-scattered electron (BSE)-SEM images of sample southeast (SE)-8 from the interlayer between the lower and middle ore beds. Images show hematite with Mn-carbonate along the rim of detrital quartz. Bottom figs: Energy dispersive spectrum (EDS) maps of relative Si, Mn, Fe and Al content (left to right, respectively) from the region indicated in panel (c). Scale bars represent 100 μm.

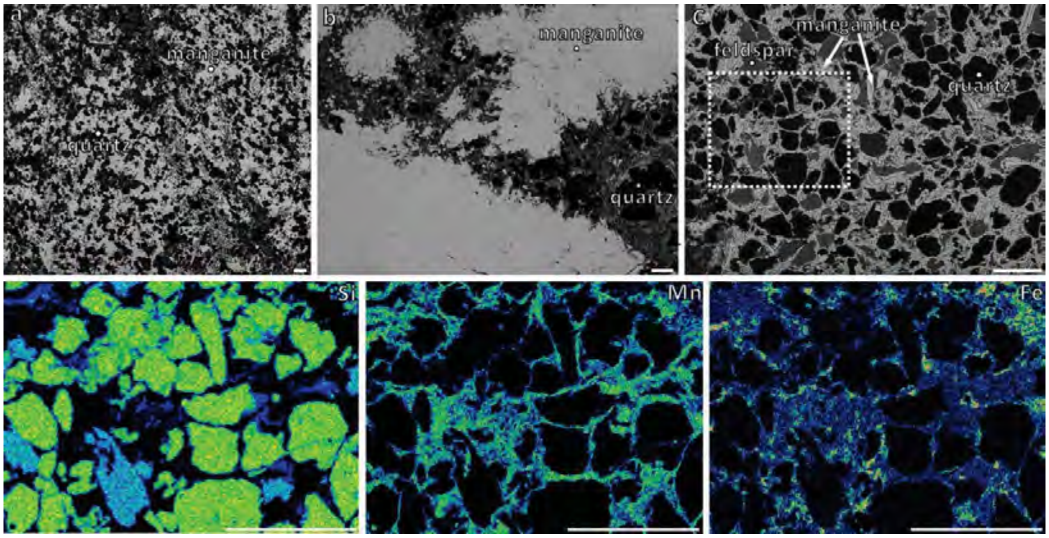

Fig. 12: Back-scattered electron (BSE)-SEM images of samples southeast (SE)-9 and 10 from the middle ore bed. (a-b) SE-9 showing the wide distribution of manganite in this massive ore rock. (c) SE-10 showing manganite with some Fe content present between detrital grains. Bottom figs: Energy dispersive spectrum (EDS) maps of relative Si, Mn and Fe content (left to right, respectively) from the region in panel (c). Scale bars represent 100 μm.

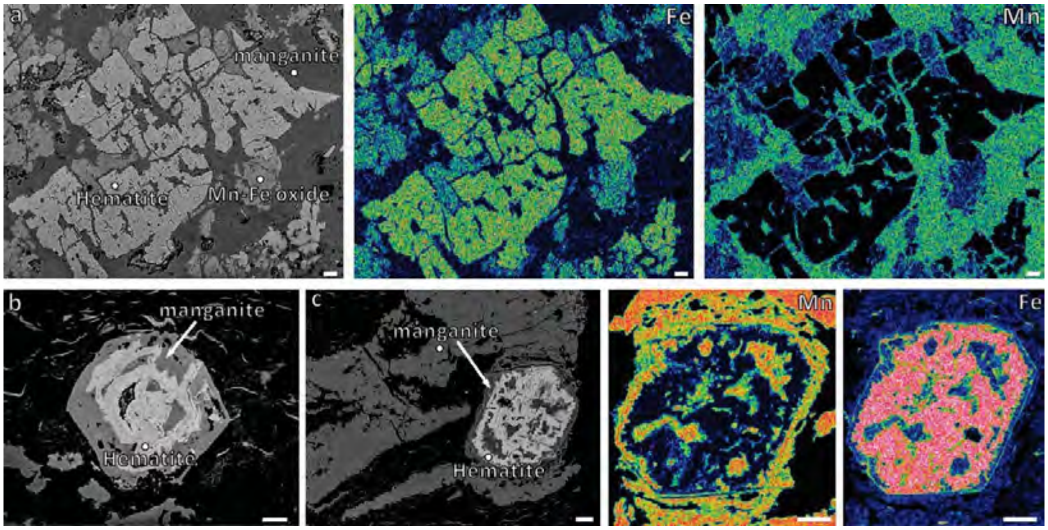

Fig. 13: Back-scattered electron (BSE)-SEM images of samples southeast (SE)-11 and 12 from the middle ore bed. (a) SE-11 is characterized by a mixed oxide phase with both Mn and Fe content observed in close association where they are present as manganite and hematite minerals, respectively. The top middle and right images are energy dispersive spectrum (EDS) maps of relative Fe and Mn content, respectively, from the region in panel (a). (b-c) SE-12 showing a clear paragenetic relationship between manganite and hematite. Bottom right images showing EDS maps of relative Mn and Fe content, respectively, from the grain in panel (c). Scale bars represent 10 µm.

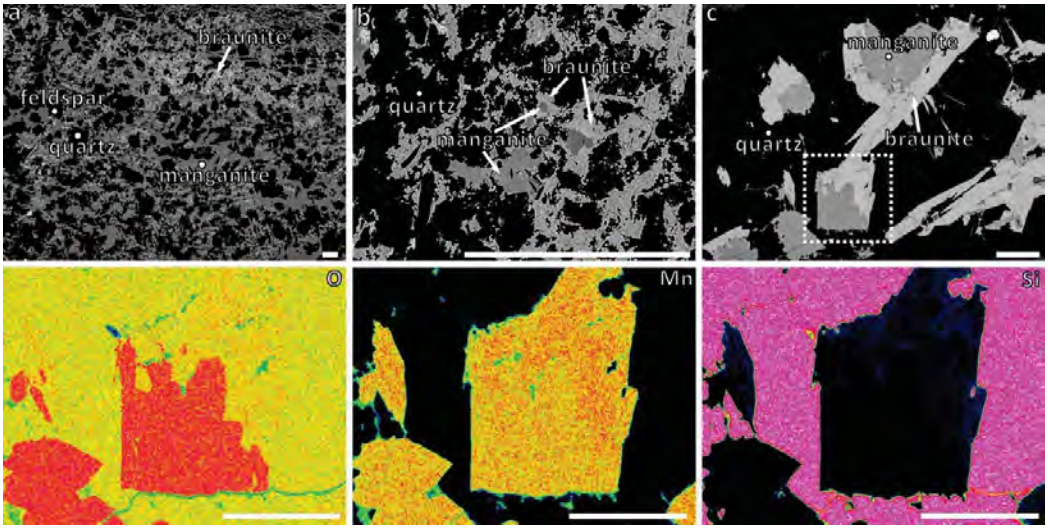

Fig. 14: Back-scattered electron (BSE)-SEM images of samples southeast (SE)-13 and 14 from the upper ore bed. (a) SE-13 showing manganite and braunite minerals phases in this massive ore rock. (b-c) SE-13 and 14 both showing the replacement of manganite by braunite, appearing to be patchy and incomplete, with relict manganite observed. Bottom figs: Energy dispersive spectrum (EDS) maps of relative O, Mn, and Si content, respectively, from the region in panel (c). Scale bars represent 100 μm.

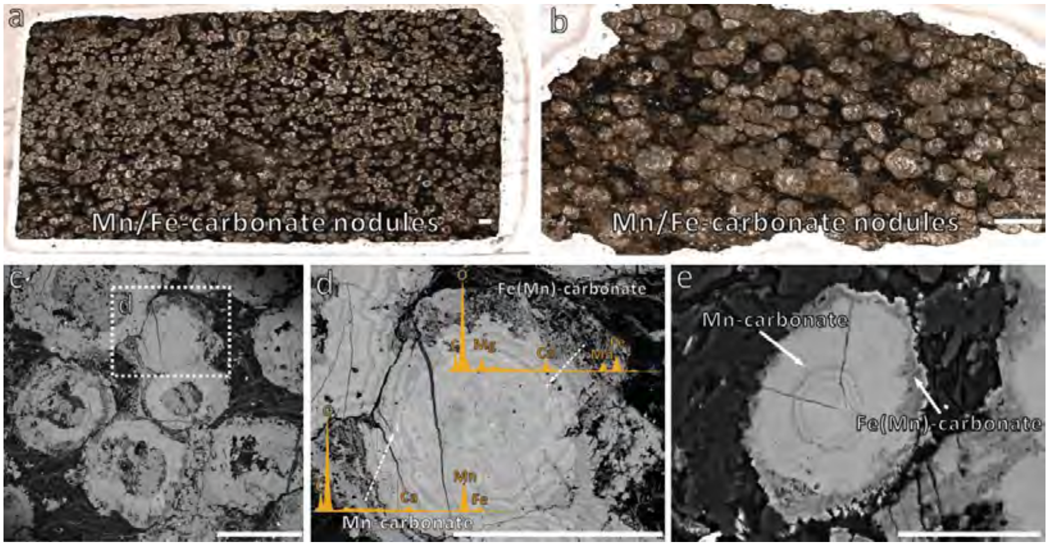

Fig. 15: (a-b) Transmitted light images of samples northwest (NW)-2 and 3 from the lower ore bed showing the wide distribution of Mn/Fe-carbonate nodules. (c-e) Back-scattered electron (BSE)-SEM showing the typical diagenetic concentric rings. The difference in ring color (grey and darker grey) is a reflection of the Mn:Fe ratio within Mn-Fe carbonate phases, representing Mn-carbonate and Fe(Mn)-carbonate phases, respectively, as corroborated by EDS analyses. Scale bars represent 500 μm.

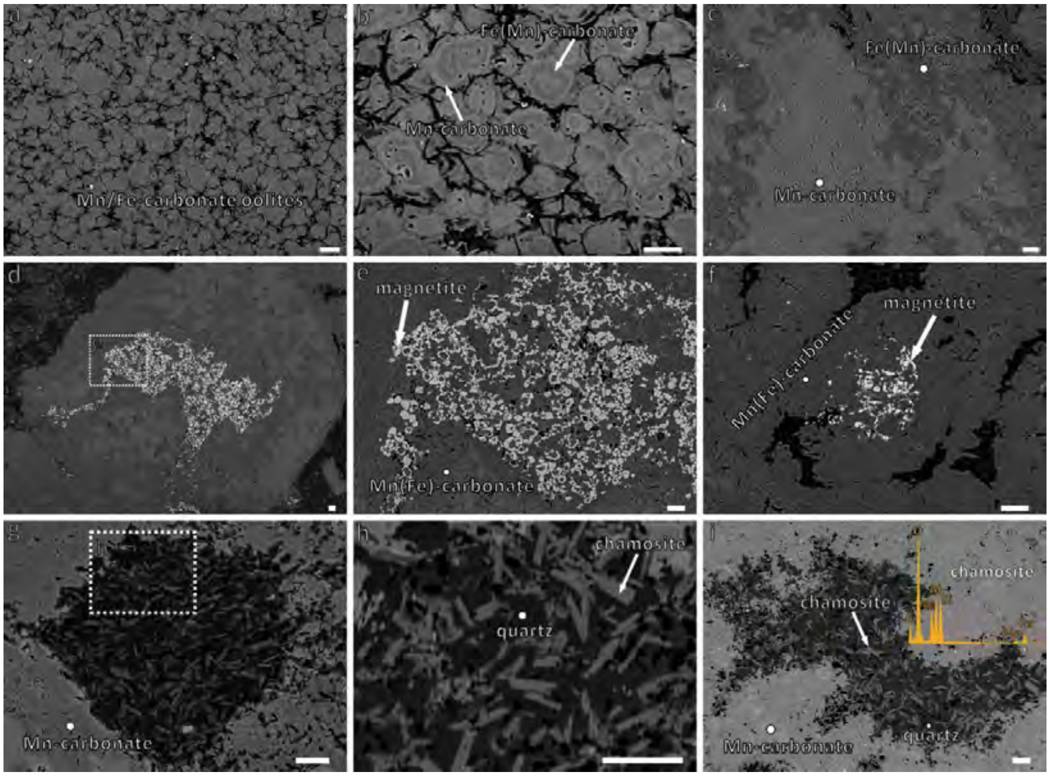

Fig. 16: Back-scattered electron (BSE)-SEM images of samples northwest (NW)-4, 5, and 6 from the middle ore bed. (a-b) NW-4 showing concentric rings of Mn-carbonate and Fe(Mn)-carbonate . (c-f) NW-5 showing the wide distribution of Mn- and Fe(Mn)-carbonate in massive ore rock. A small number of magnetite grains are replaced by Mn-Fe carbonate, with some residual magnetite preserved. (g-h) NW-6 showing abundant, randomly oriented platy chamosite particles enclosed in quartz. These sub-micron-sized particles display face-to-face and face-to-edge (“cardhouse”) contacts. Scale bars represent 10 μm.

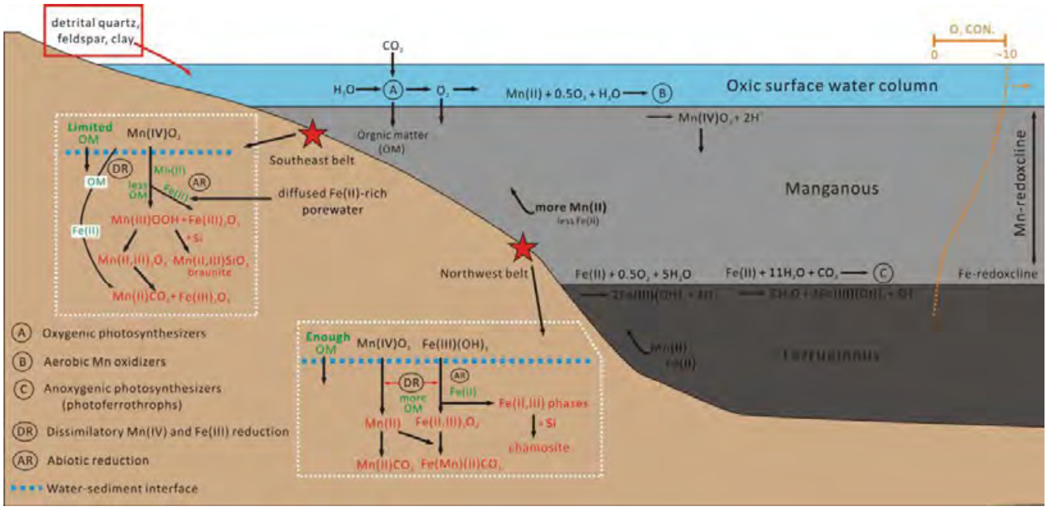

Fig. 17: Seawater redox conditions and Mn-Fe-C cycling in marine environments during deposition of the Wafangzi manganese deposit. Deposition likely occurred through the oxidation of Mn(II) in a redox-stratified water column, where a manganous water layer may have existed between shallow oxygenated water and deeper ferruginous waters. Primary Mn(IV)-oxides precipitated when aqueous, hydrothermally-derived Mn(II) was upwelled from deeper anoxic waters onto the shelf with relative high oxygen concentrations (likely $[O_2] > 10$ μM). The precipitation of Fe(III) (oxyhydr)oxide minerals may have begun under lower oxygen conditions, or even anoxic conditions via photoferrotrophy. Thus, with the progressive removal of Fe(III)-(oxyhydr)oxides, upwelling waters became relatively enriched in Mn and depleted in Fe, resulting in the elevated Mn/Fe ratios that develop between the deeper NW to shallower SE belt. In addition, the shallower SE belt captures Fe textures more indicative of porewater processes. After Mn- and Fe- (oxyhydr)oxide phases settled onto the seafloor, differences in the mineral assemblage reflect the differential flux of organic matter to the sediment pile during deposition, with more organic matter being delivered to the deeper environments to the NW. The greater delivery of organic carbon would have fueled a higher degree of dissimilatory Mn(IV) and Fe(III) reduction, and is reflected by the prevalence of Mn(II)-carbonates in the NW ore belt and preservation intermediate valence Mn minerals in the SE ore belt.